Correlation of Finite Element Analysis to Impacted Composite Plates

by

Jessica Lynn Berry

Department of Civil and Environmental Engineering
Duke University

Date: _____

Approved:

_____
Tod A. Laursen, Advisor

_____
John E. Dolbow

_____
Tomasz A. Hueckel

Thesis submitted in partial fulfillment of the requirements for the degree of
Master of Science in the Department of Civil and Environmental Engineering
in the Graduate School of Duke University
2011

Abstract

(civil engineering, mechanical engineering)

Correlation of Finite Element Analysis to Impacted Composite Plates

by

Jessica Lynn Berry

Department of Civil and Environmental Engineering
Duke University

Date: _____

Approved:

_____
Tod A. Laursen, Advisor

_____
John E. Dolbow

_____
Tomasz A. Hueckel

An abstract of a thesis submitted in partial fulfillment of the requirements for the degree of Master of Science in the Department of Civil and Environmental Engineering
in the Graduate School of Duke University
2011

"This information product has been reviewed and approved for public release. The views expressed herein are those of the author and do not reflect the official policy or position of the Department of the Army, Department of Defense, or the U.S. Government."

Abstract

The purpose of this thesis was to examine progressive composite damage models available within LS-DYNA and to correlate the results of these models with drop weight impact testing and with the non-destructive evaluation techniques of shearography, thermography, and ultrasonic testing. The secondary purpose of this study was to assess whether shearography and thermography provide an adequate less expensive replacement to ultrasonic testing. For this investigation, three models were chosen: Chang-Chang, Chang-Chang + Tsai-Wu, and a Faceted Failure Surface Model. For the experimental impact testing, two sets of specimens were chosen: a 16-ply lay-up and a 32-ply lay-up of carbon fiber pre-preg material. The panel specimens were tested at various impact energies and the displacement and force history of the impactor were recorded. The models showed good correlation for the force history with the experiments. Furthermore, the 16-ply models correlated well with the displacement history. However, due the penalty method implementation, the 32-ply models did not show similar peak displacement output. The damage shown by the models was compared to non-destructive evaluation techniques. The shearography and thermography showed significantly less damage than the ultrasonic scans, and therefore do not provide an adequate replacement to ultrasonic scanning. In looking at correlation between the models and the non-destructive evaluation techniques, the faceted failure surface showed significantly more damage due to its elastic-plastic type formulation.

This thesis is dedicated to my mother and my father, who through showing me constant, unconditional love, even when I did not deserve it, have always encouraged me to pursue my dreams and to work diligently. It is through their example that I have been molded into who I am today; and for that I am eternally grateful.

Contents

List of Tables

List of Figures

List of Abbreviations and Symbols

Symbols

α_1	User Input Parameter between 0-0.5 for Chang-Chang Failure.
α_2	User Input Parameter between 0-1.0 for Faceted Failure Surface.
β	User Input Parameter between 0-1.0 for the Chang-Chang Failure Surface.
$\mathbf{C}(\omega)$	Damage Stiffness Matrix.
E_1	Longitudinal Young's Modulus.
E_2	Transverse Young's Modulus.
f	Failure locus.
F_i,F_{ij}	Strength Parameters for the Tsai-Wu Failure Surface.
G_{12}	Shear Modulus.
$\mathbf{H}(\omega)$	Damage Compliance Matrix.
ν_{12},ν_{21}	Poisson's Ratios.
σ_1,σ_{11}	Stress in the Longitudinal Direction.
σ_2,σ_{22}	Stress in the Transverse Direction.
σ_4,σ_{23}	Shear Stress in the 23-direction.
σ_5,σ_{13}	Shear Stress in the 13-direction.
σ_6,σ_{12}	Shear Stress in the 12-direction.
S_c	Longitudinal Shear Strength.
S_t	Transverse Shear Strength.

$\bar{\tau}$	Non-linear Shear Stress Term for the Chang-Chang Failure Surface.
X_c	Longitudinal Compressive Strength.
X_t	Longitudinal Tensile Strength.
Y_c	Transverse Compressive Strength.
Y_t	Tranverse Tensile Strength.

Abbreviations

KW RWML	Kiowa Warrior Reduced Weight Missile Launcher
MDA	Missile Defence Agency
MSC	Materials Sciences Corporation
NDE	Non-desctructive Evaluation
SG	Shearography
TG	Thermography
UT	Ultrasonic

Acknowledgements

I would like to acknowledge Dr. Tod Laursen, for his guidance and leadership through the last few years as an advisor. I am glad to have been able to be his student and to have been given lessons that I can carry throughout my career. Also, I wish to express gratitude to Dr. John Dolbow for his continued help and assistance in the Computational Mechanics Lab at Duke. I am glad that he has always been approachable and offered solid advice to me.

I would like to express thanks to each of the students and the post-doc working in our lab: Justin Pogacnik, Jessica Sanders, Terence Wallace, Anand Embar, Temesgan Kindo, Chandrasekhar Annavarapu, Matthias Mayr, Hari Shanker, Wen Jiang, Martin Hautefeuille. I am honored to work around such a considerate group of individuals who have shown great willingness to help me and to help each other.

I would like to thank Sandia National Laboratories in providing partial support through a project grant to complete my Master's thesis. I am grateful to have been able to work on the Sandia project. Through this project I was able to gain a solid foundation into the basics of Finite Element Analysis and contact mechanics. Also, I wish to acknowledge Duke University Civil and Environmental Engineering Department for their support in funding the remainder of my Master's thesis work. The support staff and faculty have been a great help throughout my career at Duke University.

I would also like to thank Mr. Devlin Hayduke, Dr. Simon Chung, and Dr. Jaco

Schutte for their help in obtaining the experimental results for the this work. Lastly, I would like to thank Mr. Matt Triplett, Mr. Taylor Owens and Mr. Bob Evans for their assistance with my thesis. Each of their input and help over the years has allowed me to gain a considerable amount of knowledge and training in regards to modeling composite materials. They have been the inspiration for my thesis work and for my future research interest.

1

Introduction

Fiber composite materials provide an optimal strength to weight ratio for design. Therefore, these materials are well suited to being incorporated in military applications to make current systems "stronger, lighter, and cheaper," than their previous metal counterparts. Although these materials yield reduced weight structures, impact damage, even low-velocity impact damage occurring during normal shipping and handling, can lead to localized damage such as fiber breakage or delamination. For example, loads as small as 4 ft-lb have been shown to reduce the strength of a thin-walled cylindrical composite pressure vessel by as much as 80% (Owens and Jr., 2010). Due to this vulnerability to damage, it is essential to develop methods to assess and predict failure and to modify designs to mitigate damage.

As a part of this assessment process, accurate finite element prediction of progressive failure can reduce the cost and time of a new design and aide with quality control (Yoder et al., 2004). Currently several commercial failure models exist based on many initial ply failure criterion and progressive failure models, some of which are phenomenologically based. However, the World Wide Failure Exercise and others have shown that the models are at best loading specific in their ability to provide

adequate prediction of failure (Hinton et al., 2004). The purpose of this study is to assess currently available commercial failure models and evaluate their prediction capability in regards to the carbon fiber pre-peg material used in the Kiowa Warrior Reduced Weight Missile Launcher (KW RWML) system. Specifically, the study examines correlation of impact damage and non-destructive evaluation (NDE) techniques at various impact energies.

Failure within fiber composite laminate structure is defined on the ply level. Typically, the stress and strain present on each ply in the lay-up is calculated using lamination theory. Then, using the ply stress or ply strain, an initial ply failure criterion is applied to determine if the yield locus is exceeded. This study focuses on the following initial ply failure criterion: Chang-Chang, Hashin, Hashin-Rotem, Tsai-Wu, Max Stress, and variations of these. Once, initial ply failure occurs, the properties of the ply are reduced to allow for progressive failure of the laminate. Each of these aspects will be discussed in detail in Chapter 2.

The KW RWML was based on the objective to reduce the weight of a previous metal design, given in Figure 1.1. This system is a missile launcher that the soldier must hold and aim in battle. From the figure, the system consists of a hardback component and rails. The metal design of the hardback component weighs 41.0 lb. and the rails weigh 12.5 lb. Therefore, when added with the weight of the soldier's gear, the total weight is approximately 100 lb. The new composite system was designed using a pre-preg carbon fiber material, given in Figure 1.2. This system provides a significant weight reduction to the soldier, with the hardback having a weight savings of 29 lb. and the rails weight savings of 7 lb.

Although, the carbon fiber composite design provides optimal weight reduction, behavior of the material behavior within a field environment is crucial to determine. As stated earlier, the prediction of strength reduction of composite material is an essential design component to assess system life and in particular strength reduction

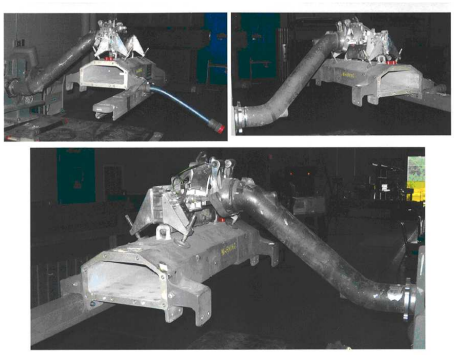

FIGURE 1.1: KW RWML Metal Design

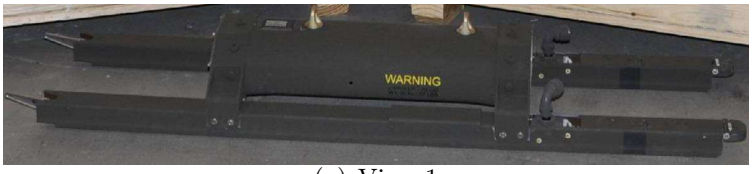

(a) View 1

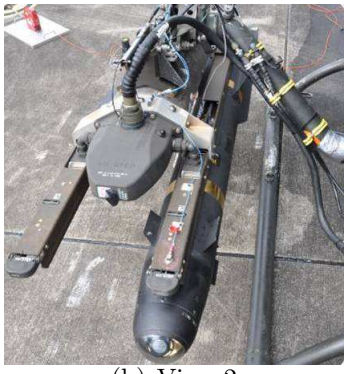

(b) View 2

FIGURE 1.2: KW RWML Composite Design

caused by the material's reaction to possible frag impact, drop loading, or other types of impact loading. For this reason, this study analyzes the effects of a impact test on 6 in. by 4 in. square panels of the carbon fiber composite material in the KW RWML. Furthermore, the study looks at the correlation between an impact and three NDE techniques, shearography, thermogrpahy, and ultrasonic testing with finite element output. All of the NDE techniques, can be used to measure the damage area. Each of these techniques will be discussed in detail in Chapter 3. The primary goal of these types of damage studies is to determine and improve upon the accuracy of the finite element prediction with experimental results, and in turn, use the associated prediction along with a structural health monitoring system to improve design and

to improve quality control criterion for a system.

1.1 Literature Review

Currently a significant body of research is available in regards to progressive composite failure theory. Specifically, as mentioned earlier, the World Wide Failure Theory sought to characterize several progressive composite failure theories that were submitted through comparison with a range of experimental results. The findings are stated in terms of recommendations relating the strengths and weaknesses of each theory, as well as, guidance to which applications are suitable for each theory. In general the consensus is that no one theory was able to perform to an acceptable manner in all the test cases presented (Hinton et al., 2004). Of key interest to this work is the implementation of currently available theories within commercial software and the accurate assessment of damage in relation to localized impact. Of secondary interest is the ability of correlate the prediction between finite element output and experimental result in order to develop a structural health monitoring system.

A study presented at the 10th International LS-DYNA Users Conference examined the effect from impact damage using a DYNATUP 8250 drop tower at varying impact energy levels on basket weave woven-roving FGI 1854 E-glass fabric and plain weave woven-rovering AS4 carbon fabric. This study compared the load displacement curves reported using an orthotropic elastic material model. In the case of the E-glass and carbon materials, the agreement between the impact load and the experimental results for the lower impact energy levels, 64 ft-lb and 128 ft-lb for the carbon material and 128 ft-lb and 256 ft-lb for the E-glass, is within approximately 100 lbf or less for each material. At the higher impact energies, 320 ft-lb and 384 ft-lb for the carbon and 640 ft-lb and 768 ft-lb for the E-glass, the difference in the carbon is about 600 lbf and approximately 400 lbf in the E-glass. This high difference in result is due to the material model not accurately incorporating the load carrying

capacity of the laminate (Thatte et al., 2008).

Nguyen *et. al.* conducted a study examining barely visible impact damage of an impacted carbon-fiber stiffened panel. The study compared three packages LS-DYNA, MSC.Dytran, and Pam-Shock. The study modeled the stiffened panel using shell elements with an impactor modeled as a hemispherical infinitely rigid member. The failure theories examined were the Chang-Chang in LS-DYNA and MSC.Dytran and the bi-phase model was used in the Pam-Shock Theory. The impact examined was a 40 J impact energy. This study found reasonable agreement between the impact energy level in regards to shape and peak force. However, the contact time was less than the experimental results which the authors attribute to the choice of modeling the end boundary conditions. This study also compared the post-failure damage area averages. (Note the exact type of experimental determination used is not explicitly stated, and only the experimental average is given.) The experimental average was given to be 775 mm^2, with LS-DYNA having an average of 1372 mm^2, MSC.Dytran having an average of 1200 mm^2, and the Pam-Shock code having an average of 6035 mm^2. The significant difference in the bi-phase damage was attributed to the bi-phase model not assuming an elastic zone before initial failure (Nguyen et al., 2005).

Okafor *et. al.* examined AS4/PEEK composite plates impacted with a steel ball fired from a gas gun. The study sought to assess damage based on broadband wave-based acoustic emission sensors, ultrasonic C-scans, and shearography. Their results show that the shearography testing provides a fast assessment of the damage in the structure, while the ultrasonic C-scans provide a more accurate picture of the damage extent. The most significant result of this study is that it demonstrates the ability to correlate the onset of damage and the damage extent, to multi-sensor information, and hence develop integrated Structural Health Management techniques (Okafor et al., 2001).

Cawley compared thermography, ultrasonic scanning, and shearography to a lamb wave inspection. His study concluded that the ultrasonic testing is the most sensitive of the three common non-destructive techniques, but is also the most expensive. For thermorgraphy and shearography scans, he stated that these methods were a function of defect diameter/depth ratio, so they will not detect small defects in comparison to ultrasonics. However, both methods are less expensive than ultrasonics. Furthermore, Crawley suggested that the lamb wave testing needed improvement before an adequate comparison could be made (Cawley, 1994).

Although, progressive failure model comparison and NDEs are extensively presented in literature. There is no study to date based on the type of carbon fiber pre-preg material used on KW RWML in relation to impact damage. Therefore, this study seeks to verify the ability of the currently available commercial software to assess this specific material.

2

Numerical Implementation

2.1 Material Models

There are a variety of material subroutines to model plasticity in fiber composite materials. For this study, LS-DYNA was used to model the impact damage. In this program, these subroutines focus on six different ways to define the failure surface: Chang-Chang, Faceted Failure Surface, Ellipsodial Failure Surface, Hashin, Hashin-Rotem, and Tsai-Wu. A brief overview of each of the material models within LS-DYNA is given in Table 2.1, and an in-depth description of each failure envelope is given the subsequent sections. Note in all the section describing the material models, the common composite convention is used for the orientation, with the 1-direction begin along the fiber and the 2-direction begin perpendicular to the fiber. A representation of this orientation is given in Figure 2.1.

Table 2.1: Available LS-DYNA Material Models

Material Model	**Element Type Supported**	**Failure Surface Type**	**Laminated Shell Theory**	**Delamination Modeling Supported**
MAT_22	Solid/Shell	Chang-Chang	yes	yes
MAT_54	Shell	Chang-Chang	yes	no
MAT_55	Shell	Chang-Chang (Fiber)	yes	no
		Tsai-Wu (Matrix)		
MAT_58b	Shell	Hashin/Hashin-Rotem	yes	no
MAT_59a	Solid/Shell	Faceted Failure Surface	yes	yes
MAT_59b	Shell	Ellipsoidal Failure Surface	yes	no
MAT_162	Solid	Hashin	no	yes

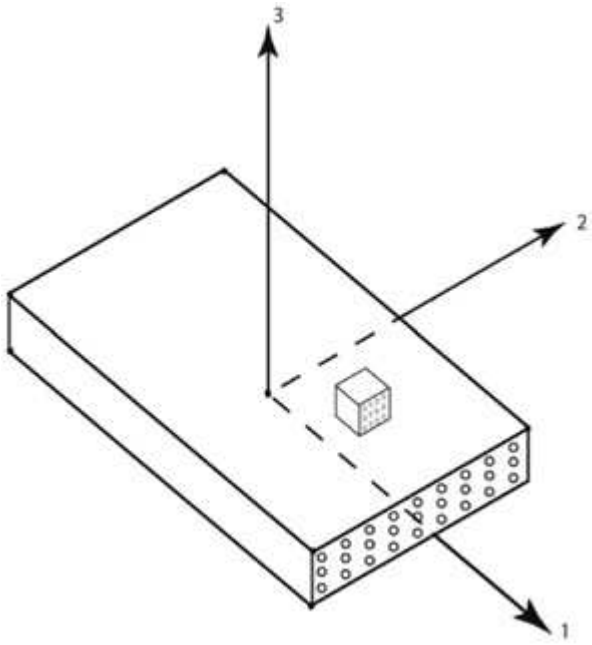

FIGURE 2.1: Fiber Coordinate System

2.1.1 Chang-Chang

This yield locus is based on experiments by Fu-Kuo Chang and Kuo-Yen Chang of bolted joints that failed in tension and shear-out and notched joints subjected to tensile load (Chang and Chang, 1987a,b). This surface is defined by four failure modes:

Tensile fiber mode (Fiber rupture) $\sigma_{11} \geq 0$:

$$f^2 = \left[\frac{\sigma_{11}}{X_t}\right]^2 + \beta\bar{\tau} \begin{cases} < 1 & \text{elastic} \\ \geq 1 & \text{failure} \end{cases} \tag{2.1}$$

In the above equation, X_t is the longitudinal tensile strength and $\bar{\tau}$ is defined as:

$$\bar{\tau} = \frac{\frac{\sigma_{12}^2}{2G_{12}} + \frac{3}{4}\alpha_1\sigma_{12}^4}{\frac{S_c^2}{2G_{12}} + \frac{3}{4}\alpha_1 S_c^4} \tag{2.2}$$

with α_1 begin a user input parameter ranging from 0-0.5 to define non-linear shear stress and S_c is the longitudinal shear strength. β is also a user input parameter. Note that if $\alpha_1 = 0$ and $\beta = 1$ then the failure is the Hashin criterion, or if $\alpha_1 = 0$ and $\beta = 0$ the failure is the Max-Stress criterion.

Compressive fiber mode (Fiber buckling and kinking) $\sigma_{11} < 0$:

$$f^2 = \left[\frac{\sigma_{11}}{X_c}\right] \begin{cases} < 1 & \text{elastic} \\ \geq 1 & \text{failure} \end{cases} \tag{2.3}$$

In the previous equation, X_c is the tranverse compressive strength.

Tensile matrix mode (Matrix cracking under transverse tension and shearing) $\sigma_{22} < 0$:

$$f^2 = \left[\frac{\sigma_{11}}{Y_t}\right]^2 + \bar{\tau} \begin{cases} < 1 & \text{elastic} \\ \geq 1 & \text{failure} \end{cases} \tag{2.4}$$

The tensile matrix mode failure is described using Y_t which is defined as the transverse tensile strength.

Compressive matrix mode (Matrix cracking under transverse compression and shearing) $\sigma_{22} < 0$:

$$f^2 = \left(\frac{\sigma_{22}}{2S_c}\right)^2 + \left[\left(\frac{Y_c}{2S_c}\right)^2 - 1\right]\frac{\sigma_{22}}{Y_c} + \bar{\tau}\begin{cases} < 1 & \text{elastic} \\ \geq 1 & \text{failure} \end{cases} \tag{2.5}$$

Note Y_c is the transverse compressive strength. Depending on which damage mode is failed differing constants in the stiffness matrix are changed. If the material fails in tensile fiber mode, then E_1, E_2, ν_{12}, and ν_{21} are set to zero. If the material fails in compressive fiber mode, then E_2, ν_{12}, and ν_{21} are set to zero. If the material fails in tensile matrix mode, then E_2, G_{12}, ν_{12}, and ν_{21} are set to zero. If the material fails in compressive matrix mode, then E_2, G_{12}, ν_{12}, and ν_{21} are set to zero. An example of the change in stiffness matrix due to compressive matrix mode is given below:

$$\begin{bmatrix} \frac{E_1}{1-\nu_{12}\nu_{21}} & \frac{E_2\nu_{12}}{1-\nu_{12}\nu 21} \\ \frac{E_1\nu_{21}}{1-\nu_{12}\nu_{21}} & \frac{E_2}{1-\nu_{12}\nu_{21}} \end{bmatrix} \xrightarrow{\text{compression damage}} \begin{bmatrix} E_1 & 0 \\ 0 & 0 \end{bmatrix} \tag{2.6}$$

Note the equation above is the traditional failure criterion given in the original paper by Chang (Chang and Chang, 1987a). Within the program environment, specifically in regards to the MAT_54 formulation, progressive failure is based on strain limitation of one of the following: maximum strain for fiber tension, maximum strain for fiber compression, maximum strain for matrix (tensile and compression), maximum shear strain, or effective strain. An example of the behavior of limiting the maximum strain in fiber tension is given in Schweizerhof, where a one element test is performed of an element in pure tension directed along the fiber direction. This test is illustrated in Figure 2.2.

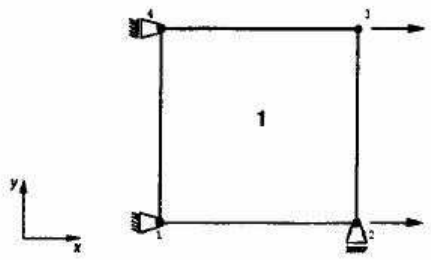

FIGURE 2.2: One Element Test (Note: The material properties are as follows: E_1 45847.0 $\frac{N}{m^2}$, E_2 17506.0 $\frac{N}{m^2}$, E_3 17506.0 $\frac{N}{m^2}$, X_t 1120 $\frac{N}{mm^2}$, X_c 900 $\frac{N}{mm^2}$, Y_t 39 $\frac{N}{mm^2}$, Y_c 134 $\frac{N}{mm^2}$, and S_c 77 $\frac{N}{mm^2}$.)

The results of this test are given in Figure 2.3. Note that once the stress in the fiber direction increases until it reaches X_t, then the fibers are breaking and in (a) the fiber stress and all the other stress is set to zero, the behavior is linear-brittle. In (b) the maximum fiber tensile strain is set to 3%, so once X_t is reached, then the material behaves elasto-plastic up to 3% tensile strain (Schweizerhof et al., 1998).

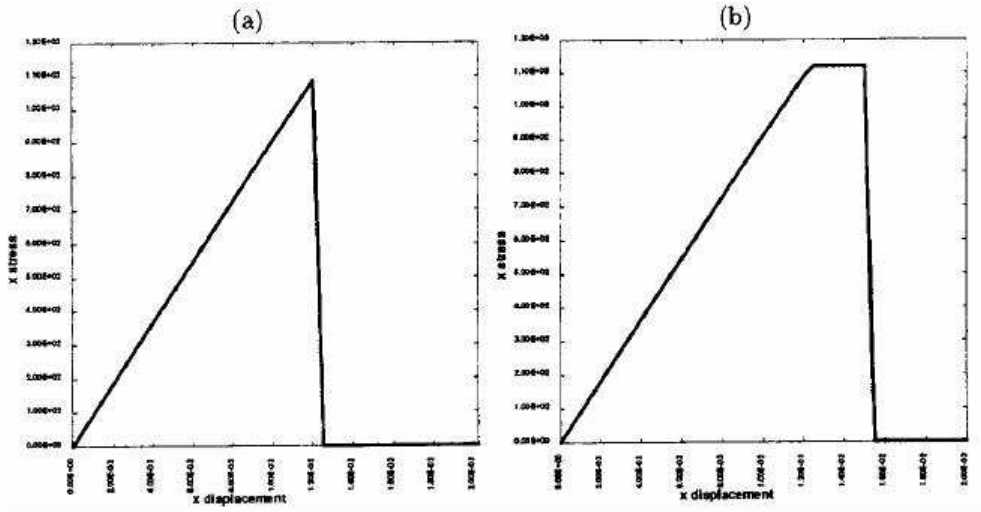

FIGURE 2.3: Stress-displacement curve for (a) 0% Maximum Fiber Tensile Strain, (b) 3% Maximum Fiber Tensile Strain

Also, with the MAT_54 formulation, progressive failure can be defined by reduction factors or either or both tensile fiber strength and compressive fiber strength. These reduction factors are applied after the matrix fails. Also, a factor called the "soft" factor may be employed which reduces the Young's modulus and strength of elements neighboring failed elements. (Note: This type of implementation models a crushing process.) The results of the same one-element test with the element loaded in the matrix direction are given in Figure 2.4

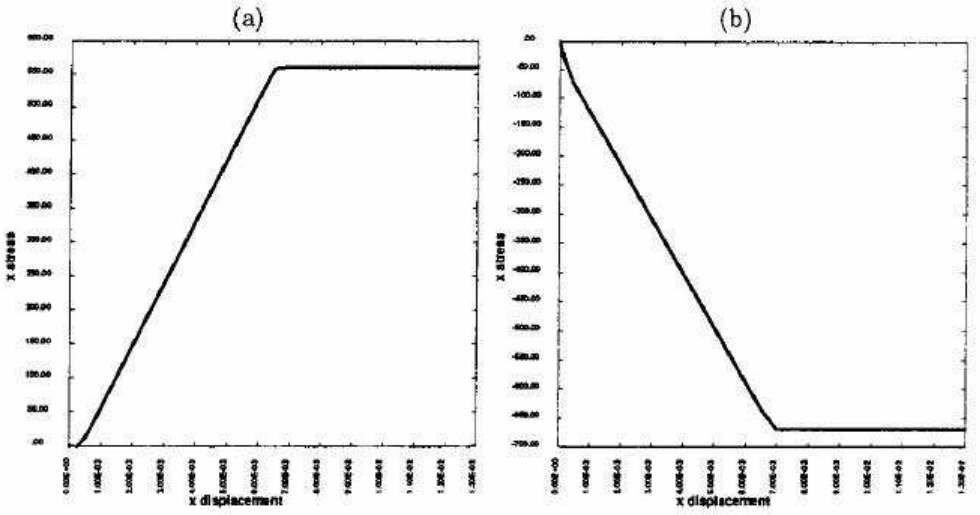

FIGURE 2.4: Stress-displacement curve for (a) Reduction Factor of Tensile Fiber Strength of 0.5 (b) Reduction Factor of Compressive Fiber Strength 5.0

The initial failure for this test is governed by Y_t and Y_c. Once the matrix fails, then the new value of X_t is given by the reduction factor times X_t for the material. Furthermore, the new value for X_c is given by Y_c times the reduction factor (Schweizerhof et al., 1998).

2.1.2 Faceted Failure Surface

Within this failure criteria, the initial ply failure is defined by the corresponding longitudinal and transverse tensile and compressive strengths and the corresponding shear strength. These yield loci are given to be:

Tensile Failure:

$$\sigma_1 = \alpha_2 X_t \tag{2.7}$$

$$\sigma_2 = \alpha_2 Y_t \tag{2.8}$$

Compressive Failure:

$$\sigma_1 = -X_c \tag{2.9}$$

$$\sigma_2 = -Y_c \tag{2.10}$$

Shear Failure:

$$\sigma_{12} = \sigma_{23} = \sigma_{13} = \pm S_c \tag{2.11}$$

where the α_2 is a user input parameter, called the strength reduction factor, ranging from 0-1 (Schweizerhof et al., 1998). After initial yielding, the next yield point is based on the equation given below:

$$\sigma_{yield} = \alpha_2(1 - SF) \times \sigma_{strength} \tag{2.12}$$

where SF is the softening factor and $\sigma_{strength}$ is the corresponding longitudinal/transverse tensile, compressive, or shear strength. (Note if α_2 is set to 1 and SF is set to zero, the material behaves in an elastic perfectly-plastic manner.)

2.1.3 Ellipsoidal Failure Surface

This failure surface is described by Equation(2.13) which is an ellipsoidal failure surface with axes parallel to the axes of orthotropy. Note that the surface is similar to the Tsai-Wu surface, but does not contain the coupling terms between the orthotropy directions (Schweizerhof et al., 1998).

$$\begin{aligned} f^2 = & \frac{4\left[\sigma_1 - \frac{X_t - X_c}{2}\right]^2}{\left(X_t + X_c\right)^2} + \frac{4\left[\sigma_2 - \frac{Y_t - Y_c}{2}\right]^2}{\left(Y_t + Y_c\right)^2} \\ & + \left[\frac{\sigma_{12}}{S_c}\right]^2 + \left[\frac{\sigma_{13}}{S_c}\right]^2 + \left[\frac{\sigma_{23}}{S_c}\right]^2 \begin{cases} < 1 & \text{elastic} \\ \geq 1 & \text{failure} \end{cases} \end{aligned} \tag{2.13}$$

Progressive failure of this surface is based on the same model as in the faceted failure surface.

2.1.4 Hashin/Hashin-Rotem

Hashin and Rotem proposed a phenomenologically based criteria based on four failure modes, tensile fiber failure, compressive fiber failure, tensile matrix failure, and compressive matrix failure (Hashin and Rotem, 1973).

Tensile fiber mode (Fiber rupture) $\sigma_{11} \geq 0$:

$$f^2 = \left[\frac{\sigma_{11}}{X_t}\right]^2 \begin{cases} < 1 & \text{elastic} \\ \geq 1 & \text{failure} \end{cases} \tag{2.14}$$

Compressive fiber mode (Fiber buckling and kinking) $\sigma_{11} < 0$:

$$f^2 = \left[\frac{\sigma_{11}}{X_c}\right]^2 \begin{cases} < 1 & \text{elastic} \\ \geq 1 & \text{failure} \end{cases} \tag{2.15}$$

Tensile matrix mode (Matrix cracking under transverse tension and shearing) $\sigma_{22} \geq 0$:

$$f^2 = \left[\frac{\sigma_{22}}{Y_t}\right]^2 + \left[\frac{\sigma_{12}}{S_c}\right]^2 \begin{cases} < 1 & \text{elastic} \\ \geq 1 & \text{failure} \end{cases} \tag{2.16}$$

Compressive matrix mode (Matrix cracking under transverse compression and shearing) $\sigma_{22} < 0$:

$$f^2 = \left[\frac{\sigma_{22}}{Y_c}\right]^2 + \left[\frac{\sigma_{12}}{S_c}\right]^2 \begin{cases} < 1 & \text{elastic} \\ \geq 1 & \text{failure} \end{cases} \tag{2.17}$$

Hashin later presented a modified form of the Hashin-Rotem criterion with different failure surfaces for tensile fiber failure and compressive matrix failure (Hashin, 1980). One of the material models examined here, MAT_58b, uses a modification of the Hashin criterion. This model is characterized by Hashin failure in the tensile fiber mode, given in Equation (2.18), and by the compressive and tensile matrix failure already presented. However, it contains a modification in the compressive fiber mode, given in Equation(2.19).

Tensile fiber mode (Fiber rupture) $\sigma_{11} \geq 1$:

$$f^2 = \left[\frac{\sigma_{11}}{X_t}\right]^2 + \left[\frac{\sigma_{12}}{S_c}\right]^2 \begin{cases} < 1 & \text{elastic} \\ \geq 1 & \text{failure} \end{cases} \tag{2.18}$$

Compressive fiber mode (Fiber buckling and kinking) $\sigma_{11} < 0$:

$$f^2 = \left[\frac{\sigma_{11}}{X_c}\right]^2 + \left[\frac{\sigma_{12}}{S_c}\right]^2 \begin{cases} < 1 & \text{elastic} \\ \geq 1 & \text{failure} \end{cases} \tag{2.19}$$

It should be noted that the above failure equations represent failure in terms of nominal stresses. In general, stress is thought of in terms of effective stress, $\hat{\sigma}_{ij}$. This

component comes from continuum damage mechanics, that only an undamaged part of a cross-section can carry load. Therefore, the effective stress is an average stress related to the net area (Schweizerhof et al., 1998). The relationship between effective stress and nominal stress is given as:

$$\hat{\sigma} = \begin{bmatrix} \hat{\sigma}_{11} \\ \hat{\sigma}_{22} \\ \hat{\sigma}_{12} \end{bmatrix} = \mathbf{M}\sigma = \begin{bmatrix} \frac{1}{1-\omega_{11}} & 0 & 0 \\ 0 & \frac{1}{1-\omega_{22}} & 0 \\ 0 & 0 & \frac{1}{1-\omega_{33}} \end{bmatrix} \begin{bmatrix} \sigma_{11} \\ \sigma_{22} \\ \sigma_{33} \end{bmatrix} \tag{2.20}$$

where the ω terms are damage parameters and ω_{11} and ω_{22} take on different values depending on tensile or compressive loading conditions. Therefore, prior to damage, $\mathbf{M}$ is the identity matrix with all ω terms begin zero, and after damage the ω terms are non-zero. From this relationship, the damaged stiffness tensor is found. Consider the compliance relationship for the damaged lamina in terms of effective stress:

$$\epsilon = \mathbf{H}_0\mathbf{M}\sigma \tag{2.21}$$

where $\mathbf{H}_0\mathbf{M}$ is given as:

$$\mathbf{H}(\omega) = \begin{bmatrix} \frac{1}{(1-\omega_{11})E_1} & \frac{-h_{21}(\omega)\nu_{12}}{(1-\omega_{22})E_1} & 0 \\ \frac{-h_{12}(\omega)\nu_{12}}{(1-\omega_{11})E_2} & \frac{1}{(1-\omega_{22})E_2} & 0 \\ 0 & 0 & \frac{1}{(1-\omega_{12})G_{12}} \end{bmatrix} \tag{2.22}$$

Based on previous work, the terms $h_{21}(\omega)$ and $h_{12}(\omega)$ are reasonably represented as:

$$h_{21}(\omega) = (1-\omega_{22})h(\omega_{11}) \tag{2.23a}$$

$$h_{12}(\omega) = (1-\omega_{11})h(\omega_{11}) \tag{2.23b}$$

$$h(\omega_{11}) = 1 \tag{2.23c}$$

giving,

$$\mathbf{H}(\omega) = \begin{bmatrix} \frac{1}{(1-\omega_{11})E_1} & -\frac{\nu_{12}}{(1-\omega_{22})E_1} & 0 \\ -\frac{\nu_{12}}{(1-\omega_{11})E_2} & \frac{1}{(1-\omega_{22})E_2} & 0 \\ 0 & 0 & \frac{1}{(1-\omega_{12})G} \end{bmatrix} \tag{2.24}$$

Inverting the expression for the compliance matrix will give the damaged stiffness tensor:

$$\mathbf{C}(\omega) = \frac{1}{D} \begin{bmatrix} (1-\omega_{11})E_1 & (1-\omega_{11})(1-\omega_{22})\nu_{21}E_2 & 0 \\ (1-\omega_{11})(1-\omega_{22})\nu_{12}E_1 & (1-\omega_{22})E_2 & 0 \\ 0 & 0 & D(1-\omega_{12})G_{12} \end{bmatrix}$$

$$\text{with } D = 1-(1-\omega_{11})(1-\omega_{22})\nu_{12}\nu_{21} > 0\text{Schweizerhof et al. (1998).} \tag{2.25}$$

For this material model, the assumed damage evolution is:

$$\omega_i = 1 - exp\left[-\frac{1}{m_i e}\left(\frac{\epsilon_i}{\epsilon_f}\right)^{m_i}\right] \tag{2.26}$$

where m_i are parameters that describe developing failure modes (tension, compression, shear) and ϵ_f is the nominal failure strain given by:

$$\epsilon_{f1} = \frac{X_t}{E_1} \text{ or } \frac{X_c}{E_1} \tag{2.27a}$$

$$\epsilon_{f2} = \frac{Y_t}{E_2} \text{ or } \frac{Y_c}{E_2} \tag{2.27b}$$

An example of this damage evolution for varying values of m is given in Figure 2.5

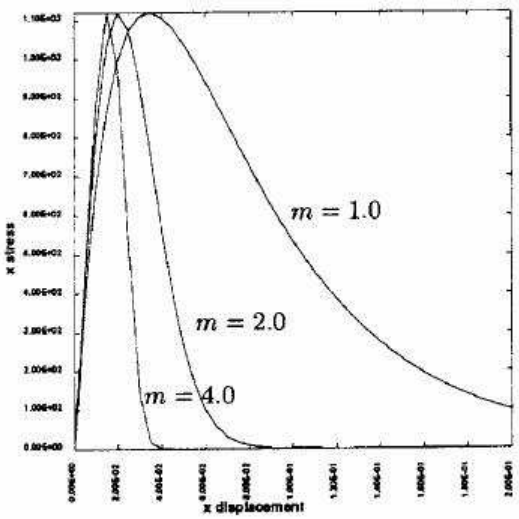

FIGURE 2.5: Stress-displacement curve for $m = 1.0$ 2.0 and 4.0

2.1.5 Tsai-Wu

This phenomenologically based, quadratic failure criterion was developed by Tsai-Wu to provide a highly simplified characterization equation for composite materials (Tsai and Wu, 1971). This criterion does not contain different yield loci for different modes of stress. The yield locus is given as:

$$f(\sigma_k) = F_i\sigma_i + F_{ij}\sigma_i\sigma_j \begin{cases} < 1 & \text{elastic} \\ \geq 1 & \text{failure} \end{cases} \tag{2.28}$$

where $i, j, k = 1, 2, ..., 6$, $\sigma_4 = \sigma_{23}$, $\sigma_5 = \sigma_{13}$, $\sigma_6 = \sigma_{12}$, and the F's are material strength parameters. For the plane stress case, this equation reduces to:

$$f(\sigma) = F_1\sigma_1 + F_2\sigma_2 + F_{11}\sigma_1^2 + F_{22}\sigma_2^2 + F_{66}\sigma_6^2 + 2F_{12}\sigma_1\sigma_2 \tag{2.29}$$

For a uniaxial ply, the strength parameters become:

$$F_1 = \frac{1}{X_t} - \frac{1}{X_c} \tag{2.30a}$$

$$F_{11} = \frac{1}{X_t X_c} \tag{2.30b}$$

$$F_2 = \frac{1}{Y_t} - \frac{1}{Y_c} \tag{2.30c}$$

$$F_{22} = \frac{1}{Y_t Y_c} \tag{2.30d}$$

$$F_{66} = \frac{1}{S_t S_c} \tag{2.30e}$$

$$F_{12} = \frac{1}{2P^2}\left[1 - P\left(\frac{1}{X_t} - \frac{1}{X_c} + \frac{1}{Y_t} - \frac{1}{Y_c}\right) - P^2\left(\frac{1}{X_t X_c} + \frac{1}{Y_t Y_c}\right)\right] \tag{2.30f}$$

where P is defined by the solution of:

$$P^2(F_{11} + F_{22} + 2F_{12}) + P(F_1 + F_2) = 1 \tag{2.31}$$

From Table 2.1, Mat_55 defines matrix failure based on the Tsai-Wu criterion. In order to define the failure in this way, the matrix is assumed to fail based on the stress perpendicular to the fiber direction, σ_2, and the shear stress. Also, the shear strength is presumed to behave the same in compressive and tensile loading. Therefore, the σ_1, in Equation(2.29) is set to zero which gives the failure surface as:

$$f(\sigma) = f^2 = \frac{\sigma_2^2}{Y_t Y_c} + \left[\frac{\sigma_6}{S_c}\right]^2 + \frac{(Y_c - Y_t)\sigma_2}{Y_c Y_t} \begin{cases} < 1 & \text{elastic} \\ \geq 1 & \text{failure} \end{cases} \tag{2.32}$$

2.2 Variational Formulation

For the models, the variational formulation may be represented as:

$$\int_{\nu_{n-1}} S_{ij}^n \Delta E_{ij} d\nu - \int_{s_\sigma} \bar{T}_i^n \Delta u_i da - \int_{s_u} S_{ij}^n n_j \Delta \bar{u}_i da = 0 \tag{2.33}$$

where the superscript n represents the current time step, S_{ij} is the Kirchoff stress, ΔE_{ij} is the incremental Green strain, T_i is the surface traction on s_σ in the previous configuration (ν_{n-1}), Δu_i is the incremental displacement, and $\Delta \bar{u}_i$ is the displacement prescribed at s_u boundary in the ν_{n-1} configuration. The Kirchhoff stress and incremental Green strain can be rewritten as:

$$S_{ij}^n = \sigma_{ij}^{n-1} + \Delta S_{ij} \tag{2.34}$$

$$\Delta E_{ij} = \Delta e_{ij} + \Delta \eta_{ij} \tag{2.35a}$$

$$\Delta e_{ij} = \frac{1}{2}(\Delta u_{i,j} + \Delta u_{j,i}) \tag{2.35b}$$

$$\Delta \eta_{ij} = \frac{1}{2}\Delta u_{k,i}\Delta u_{k,j} \tag{2.35c}$$

where σ_{ij} is the Cauchy stress. Substituting the above relations into the variational formulation gives the updated Lagrangian Formulation below:

$$\begin{aligned}\int_{\nu_{n-1}} \Delta S_{ij}\Delta E_{ij} d\nu + \int_{\nu_{n-1}} \sigma_{ij}^{n-1}\Delta\eta_{ij} d\nu = \int_{s_\sigma} \bar{T}_i^n \Delta u_i da + \\ \int_{s_u} (\sigma_{ij}^{n-1} + \Delta S_{ij})\Delta\bar{u}_i da - \int_{\nu_{n-1}} \Delta e_{ij} d\nu\end{aligned} \tag{2.36}$$

This formulation is based on the assumption that increases in loading from step to step are small enough so that linear behavior between steps can be utilized, or

$$\Delta S_{ij} = (C_{ijkl})^{n-1}\Delta E_{kl} \cong (C_{ijkl})^{n-1}\Delta e_{kl} \tag{2.37}$$

Substituting this relationship, gives the variational form as:

$$\int_{\nu_{n-1}} \Delta e_{kl} C_{ijkl}^{n-1} \Delta e_{ij} d\nu + \int_{\nu_{n-1}} \sigma_{ij}^{n-1} \Delta \eta_{ij} d\nu = \int_{s_\sigma} \bar{T}_i^n \Delta u_i da + \int_{s_u} (\sigma_{ij}^{n-1} + \Delta S_{ij}) \Delta \bar{u}_i da - \int_{\nu_{n-1}} \sigma_{ij}^{n-1} \Delta e_{ij} d\nu \tag{2.38}$$

2.3 Numerical Procedure

Therefore, the numerical procedure is as follows:

1. Increase the applied load by a small increment:

$$P^n = P^{n-1} + \Delta P \tag{2.39}$$

2. Calculate incremental strain ΔE_{ij} and stress $\Delta \sigma_{ij}$

3. Update the total stress σ_{ij}^n.

4. Calculate the in-plane stress in each ply through coordinate transformation.

5. Check to see if any initial ply failure criteria have been met.

6. If none are met, then return to Step 1, otherwise continue.

7. Stop if the laminate cannot take any more load, else continue.

8. Reduce the parameters accordingly and redistribute the laminate stresses and strains.

3

Experimental Testing

3.1 Specimen Preparation

For this study, two sets of quasi-isotropic, 6 in. by 4 in.carbon fiber pre-preg panels were made. The first set was a 16 ply laminate with a nominal thickness of 0.1025 in. and a lay-up of (45/0/-45/90/45/0/-45/90)s. The second set was a 32 ply laminate with a nominal thickness of 0.205 in. and a lay-up of (45/0/-45/90/45/0/-45/90/90/-45/0/45/90/-45/0/45)s. The lay-up of the panels was done by Missile Defense Agency (MDA). In order to make the panels, a 25 in. by 78 in. laminate was cut into three 25 in. by 26 in. plies. The 25 in. by 26 in. plies were then laid-up according to each of the laminate sequences given with a debulk occurring at every eighth layer. Debulking a panel consists of wrapping the covering the panel with Armalon, a thin perforated plastic, on both the top and bottom of the panel and placing the panel between two caul plates in ensure flatness. These plates are wrapped in breather cloth material and placed inside a vacuum bag and pressure is applied for approximately 15 to 20 minutes. After the full lay-up was complete, a final bag was placed on the part and the part was cured in the autoclave. Following

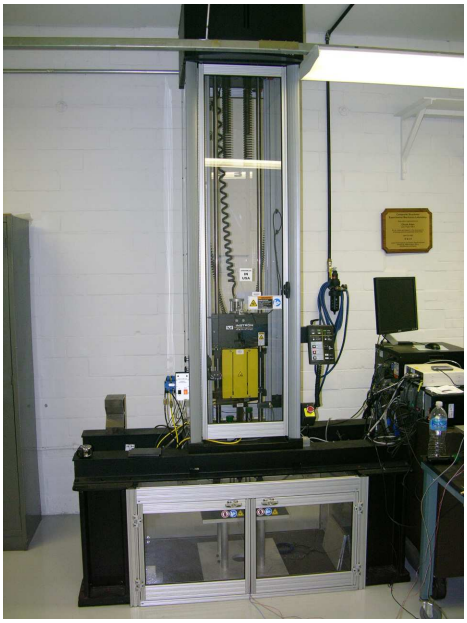

FIGURE 3.1: Impact Tower

cure, the 25in. by 26 in. panels were machined into four 12 in. by 12.5 in. panels with the 0° direction and the number of plies labeled on each. These panels were sent to Material Sciences Corporation (MSC) for waterjet cutting into 6 in. by 4 in. specimens. Note that all panels were made using a similar procedure to the one described here.

3.2 Impact Testing

Each 6 in. by 4 in. test specimen was impacted in accordance with ASTM D7136, Standard Test Method for Measuring the Damage Resistance of a Fiber-Reinforced Polymer Matrix Composite to a Drop-Weight Impact Event. A Dynatup 9250HV impact test machine was used with 5/8 in. diameter hemispherical tipped steel impactor. The specimens were mounted on a support base built by MSC from the D7136 specifications. The impact machine and the support base are shown in Figures 3.1-3.2.

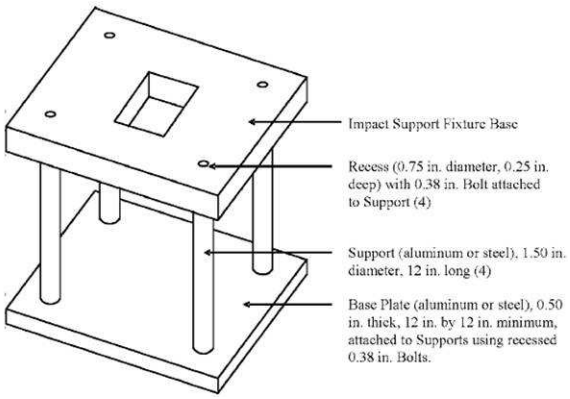

FIGURE 3.2: Support Base

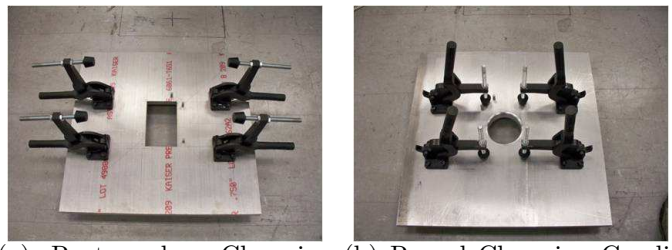

(a) Rectangular Clamping Condition with Square Edge (b) Round Clamping Condition with Round Edge

FIGURE 3.3: Impact Testing Clamping Conditions

For this study, two different clamping boundary conditions, round and rectangulular clamps, and only the square edge type were used to assess if there was any difference on the output. These clamping boundary conditions are given in Figure 3.3. The testing plan and the specimen ids are shown in Table 3.1-3.2. (Note: In these tables, the impact energy is calculated based on Equation (3.1), where m is the impactor mass, g is the gravitational constant, and h is the drop height.)

$$E = mgh \tag{3.1}$$

Table 3.1: Test Plan for 0.1025 in. Panels

Test ID	**Clamping Style**	**Impact Energy (ft-lb)**
T33	Round	5
T34	Round	7.5
T35	Round	10
T36	Round	12.5
T37	Round	2.5
T38	Round	2.5
T39	Round	7.5
T40	Round	12.5
T41	Rectangular	7.5
T42	Rectangular	12.5
T43	Rectangular	2.5
T44	Rectangular	5
T45	Rectangular	5
T46	Rectangular	7.5
T47	Rectangular	2.5
T48	Rectangular	7.5

Table 3.2: Test Plan for 0.205 in. Panels

Test ID	**Clamping Style**	**Impact Energy (ft-lb)**
T17	Round	20
T18	Round	25
T19	Round	30
T20	Round	35
T21	Round	40
T22	Round	15
T23	Round	10
T24	Round	5
T25	Rectangular	20
T26	Rectangular	25
T27	Rectangular	30
T28	Rectangular	35
T29	Rectangular	40
T30	Rectangular	15
T31	Rectangular	10
T32	Rectangular	5

The impact force history and displacement history for each impact energy level readings from the Dynatup 9250HV for both sets of specimens are given in Figures 3.4-3.10. The impact force history is measured using a strain gauge/piezo electric transducer. The position is measured using an optical encoder transducer and the weight is measured using an electrical strain guage with load cell. Also, the work done on the specimen by the tup is calculated by numerically integrating the area under the force displacment curve using the mid-point rule. An example of the numerical integration is given below:

$$W_{t_n+1} = (d_{t_n+1} - d_{t_n}) \left(\frac{F_{t_n} + F_{t_n+1}}{2} \right) + W_{t_n} \tag{3.2}$$

with t_n indicating the current time and $t_n + 1$ being the next time step, d indicating the displacement, F indicating the force, and W indicating work. Note that the work done given in the graphs can be thought of as energy absorption curves of the specimens. At time t=0 is the start of the impact event. As the impactor's velocity decreases during contact, impact energy is transferred to the specimen in the form of elastic bending and damage mechanisms. When the impactor reaches zero velocity, energy absorption is at its maximum value (Tan et al., 2010). Therefore, the peak energy is in the plots equivalent to the impact energy, the total energy introduced into the composite specimen, and the final energy in the plots is the energy absorbed by the composite specimen. (Note that a higher final energy indicates greater absorption of energy by the specimen or a less elastic collision. This can be clearly seen in Figure 3.7.) Some specifications in relation to these measurements are given in Appendix A.

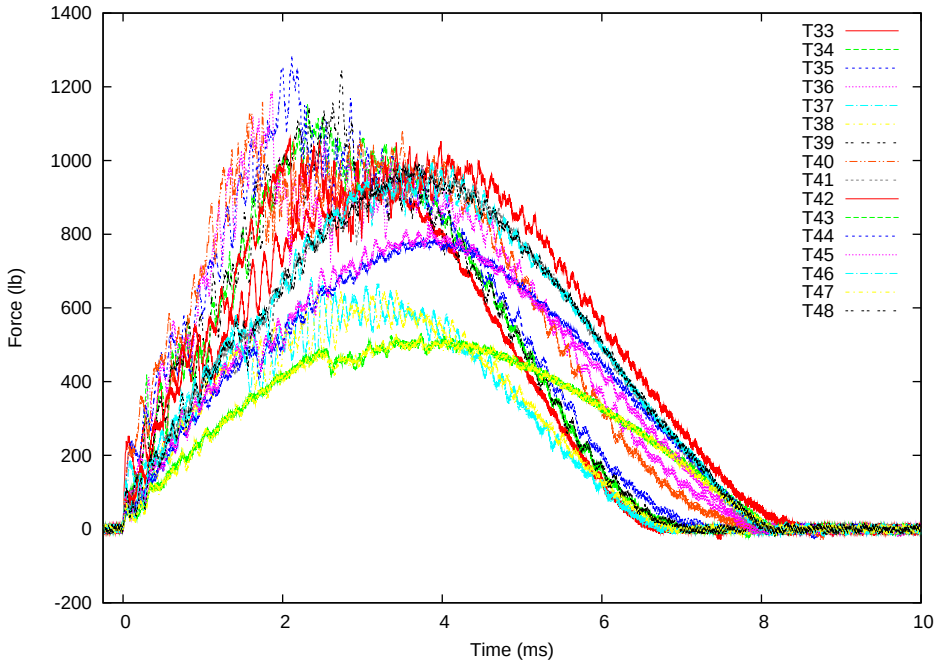

FIGURE 3.4: Force versus Time History for the 0.1025 in. Specimens

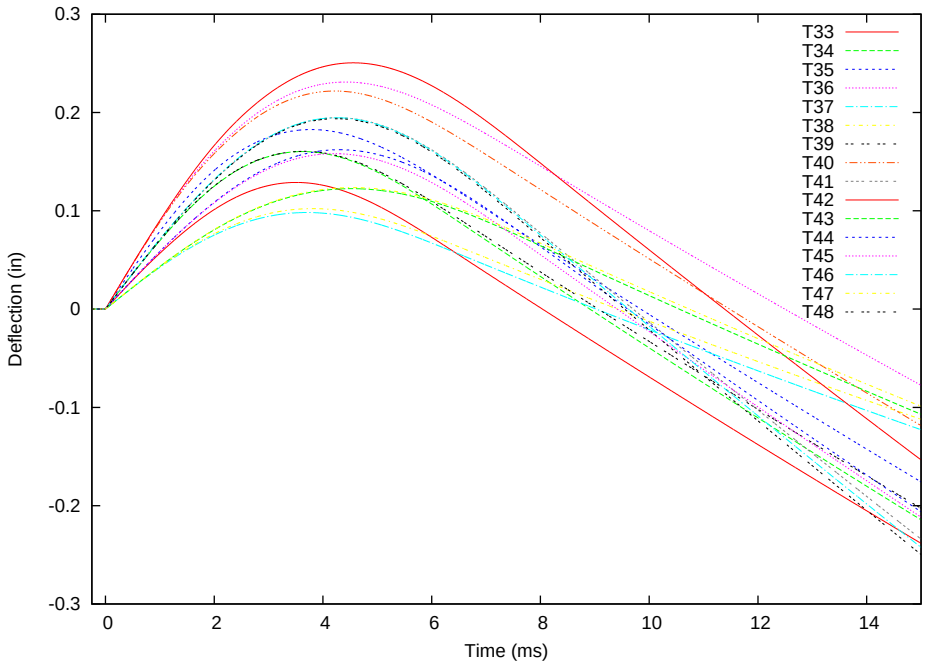

FIGURE 3.5: Displacement versus Time History for the 0.1025 in. Specimens

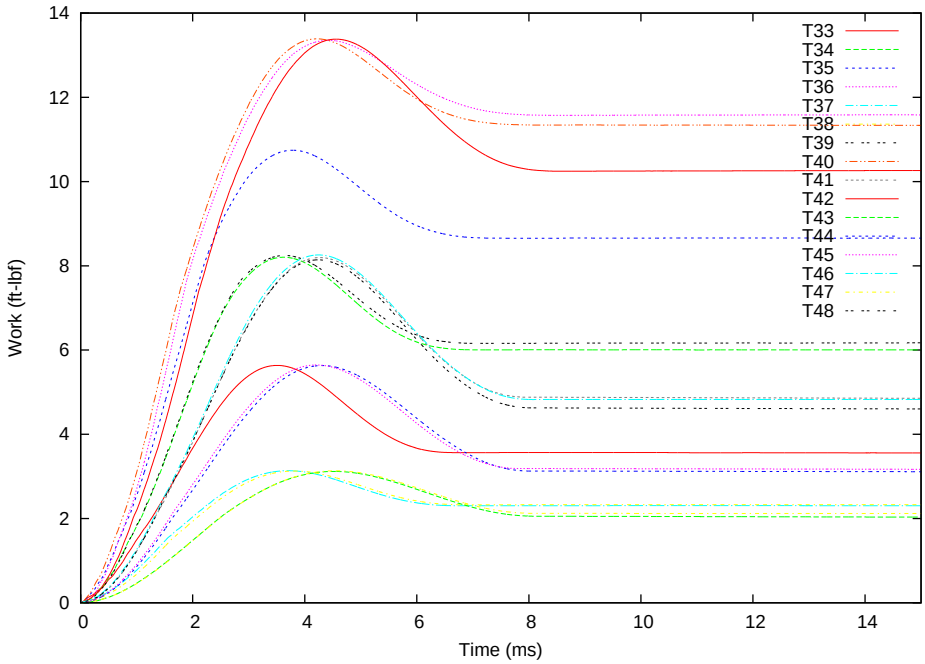

FIGURE 3.6: Work Done versus Time History for the 0.1025 in. Specimens (Note that in these plots work indicates work done by the tup on the specimen.)

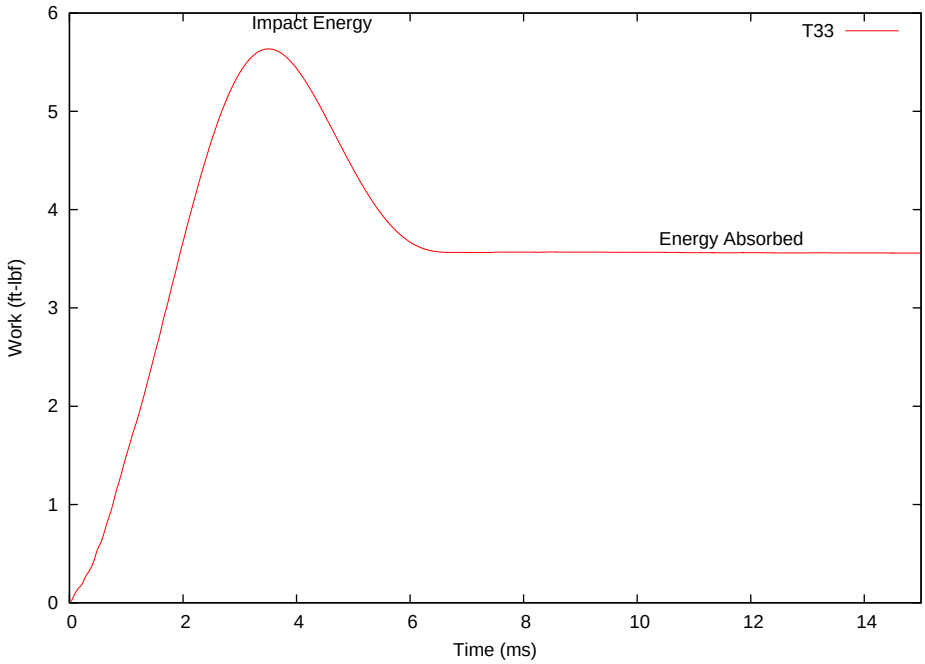

FIGURE 3.7: Explanation of the Work Done vs. Time Plots (Note: The peak is the impact energy and the leveling off value is the energy absorbed by the specimen.)

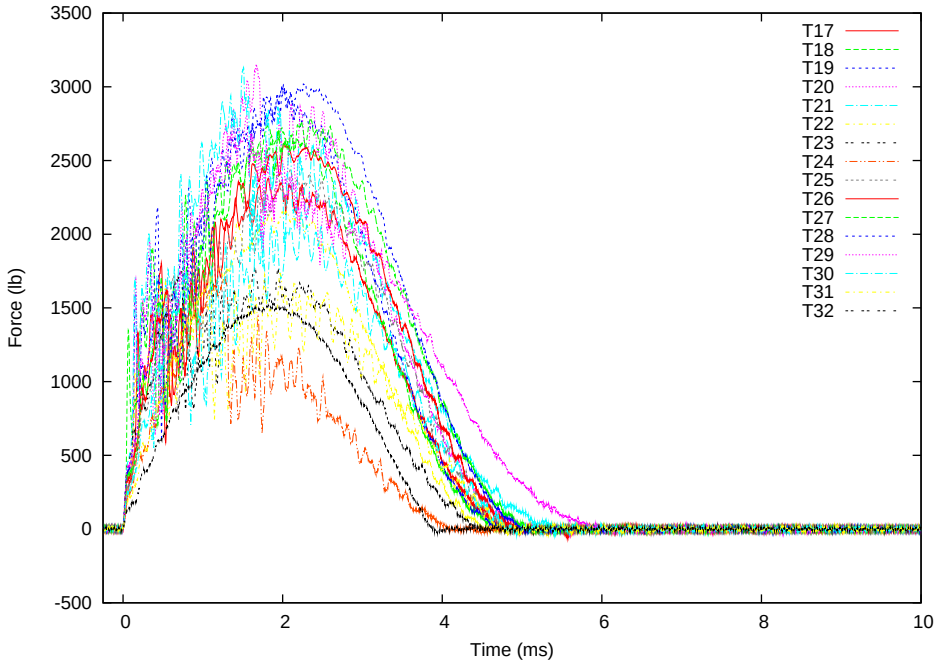

FIGURE 3.8: Force versus Time History for the 0.205 in. Specimens

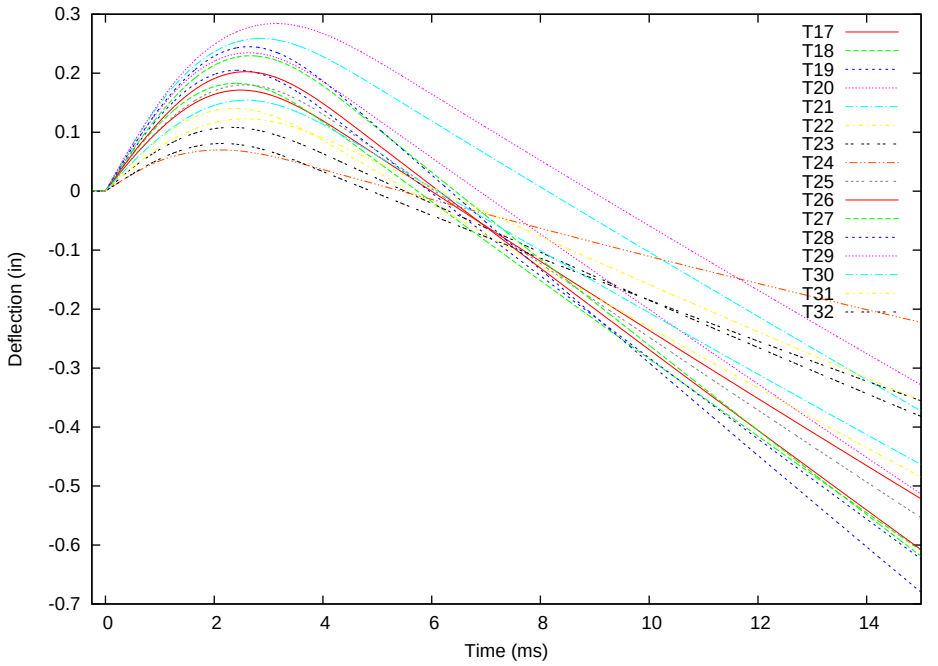

FIGURE 3.9: Displacement versus Time History for the 0.205 in. Specimens

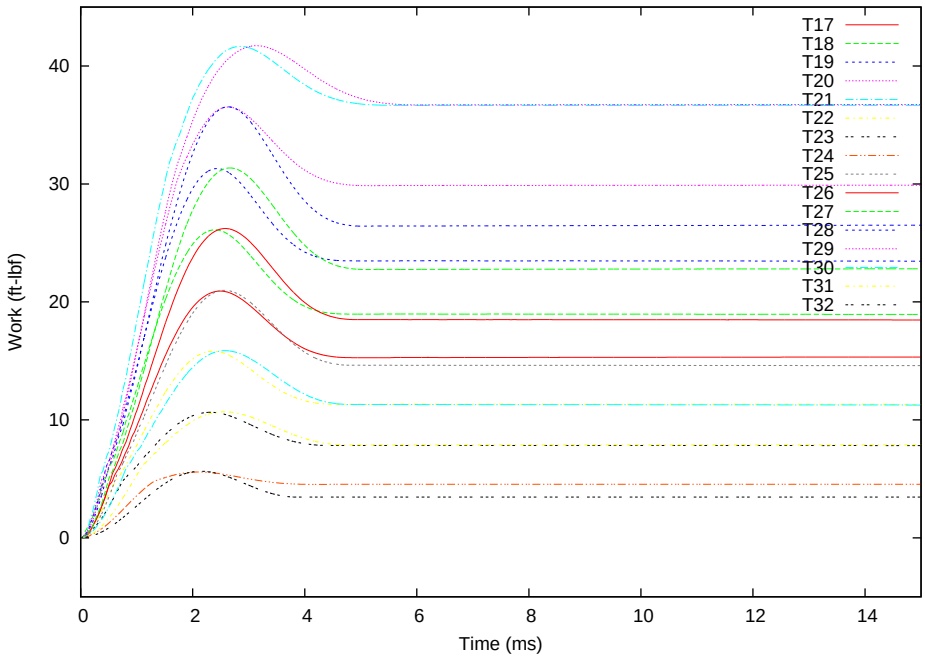

FIGURE 3.10: Work Done versus Time History for the 0.205 in. Specimens

3.3 Non-Destructive Evaluation Testing

Post impact testing three non-destructive evaluation techniques were performed on the specimens. Each is described in the subsequent sections.

3.3.1 Shearography Testing

Each impact specimen was tested using a LTI-5100 Digital Shearography System. Shearography is based on the concept of interferometry, the study of wave interference and superposition. This system uses a common path interferometer to image the first derivative of the out-of-plane deformation of a part surface in response to a change load (Incorporated, 2010). In essence, the specimen is put under a low strain load from heat, vibration, or pressure, and a change in the surface strain is caused by the presence of the fault in the material and dectected through the use of a camera (Růžek et al., 2006). (Note: An example of what is considered a low strain used during a shearography test on an impacted composite pressure vessel would be an applied pressure of 10 psi after impact, which is several orders of magnitude lower than the burst pressure of the vessel itself.)

This shearography system is based on a modification of the Michelson type inferometer, given in Figure 3.11. (Note the Michelson inferometer uses a single beam splitter to separate and recombine the light beams.) In Figure 3.12 the incorporation of the Michelson inferometer in the shearography system is seen. A sheared image, consisting of two shifted images, is generated focusing the laser beam onto the test part and tilting mirror 1 in Figure 3.12 (Steinchen and Yang, 2003). The addition of the interference of these two images and a reference image creates a fringe pattern (Incorporated, 2010).

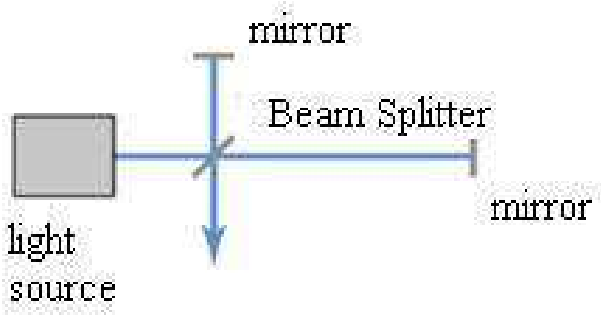

FIGURE 3.11: Michelson Interferometer

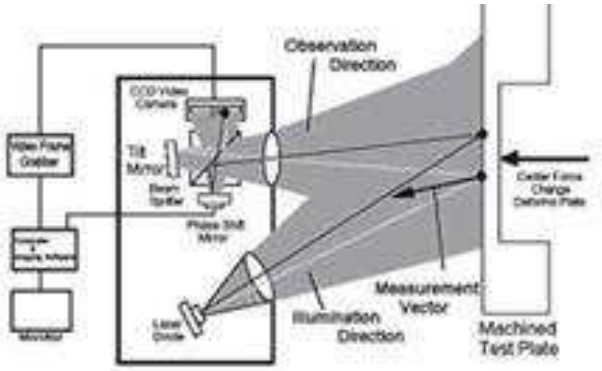

FIGURE 3.12: Schematic of Shearography System

For the impact specimens, a heat source was applied and a shearographic image was taken. The heat source applied was a heating gun which only raises the temperature within a few degrees of the of the structure. A picture of the specimen set-up is given in Figure 3.13(a) and a resulting fringe-free shearography image is given in Figure 3.14.

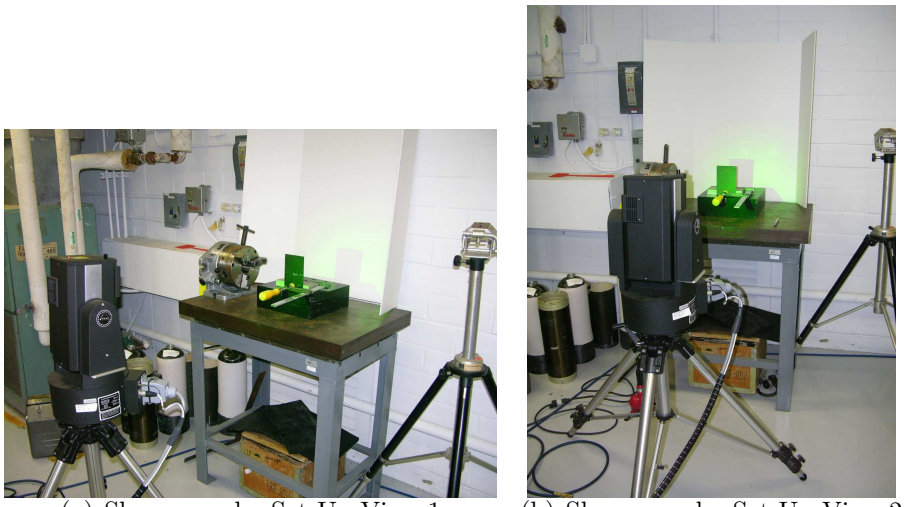

(a) Shearography Set-Up View 1 (b) Shearogrpahy Set-Up View 2

FIGURE 3.13: Shearography Set-Up

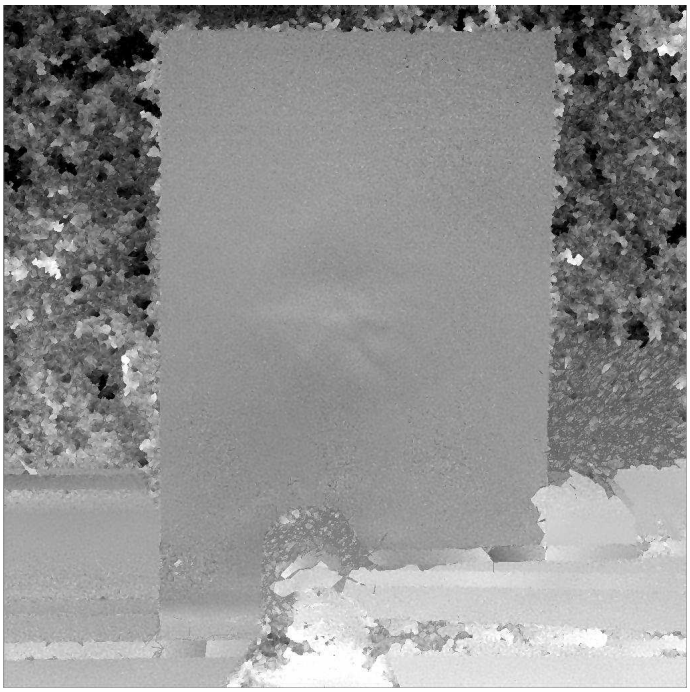

FIGURE 3.14: Shearography Image for the T17 Specimen

3.3.2 Thermography Testing

These specimens were tested using line scanning thermography. Thermography analysis looks at the temperature distribution across an object. Line scanning thermography operates by applying a infrared heat source in a line at a constant speed and distance from the object. An infrared camera coupled images the temperature of the region on the surface of the specimen. The infrared detector provides images on each side of the heat source, so each image has a baseline of the reference temperature (Products, 2010). The amount of damage or damage area is detected through the use of image data processing which calculates the spatial variations of the temperature across specimen. Since, parts of the material that have defects are thinner, having lower thermal mass, will have a higher surface temperature or diffuse heat at a slower rate the located and size of the defect may be indicated by process the thermal map (Center, 2011). (Note: This type of thermography employs passive heating, meaning that a heat source or heat sink is required to establish the flow of heat from the test object. According the standards, the only that the heating must not be instrusive. The rate of heating must be below producing the damage due to thermal stresses (Hardy and Bolen, 1989).)

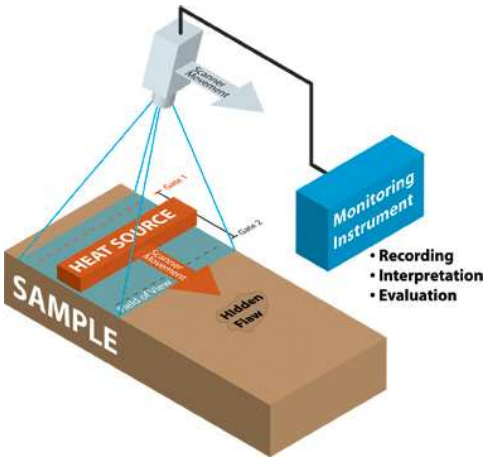

FIGURE 3.15: Thermography Operation Schematic

FIGURE 3.16: Thermography Experimental Set-up

For these specimens, eight panels were lined up in row and the scans were taken at a scanning rate of 1.5 in/s with heat intensity at 70% out of 200 W/m. An example of the experimental set-up is given in Figure 3.16.

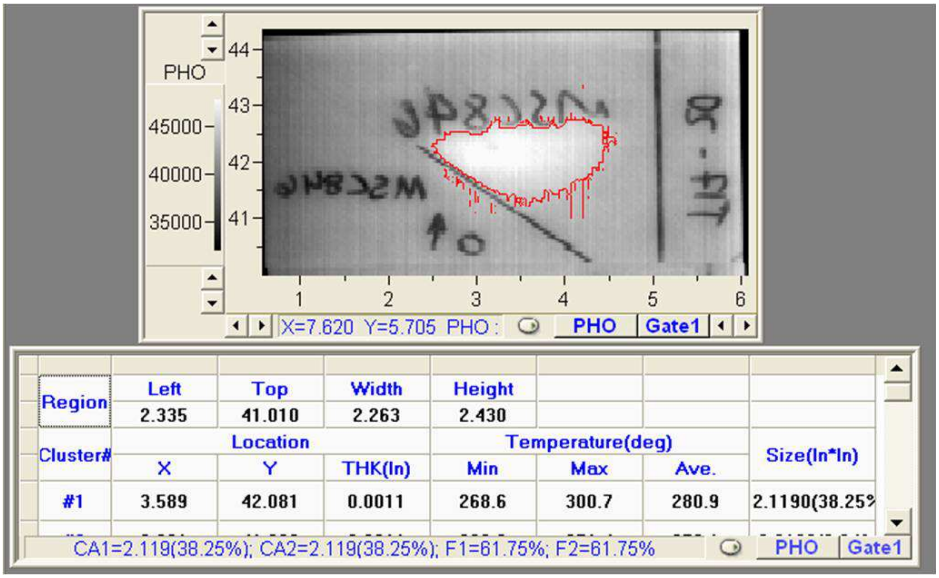

FIGURE 3.17: T17 Thermography Specimen

3.3.3 Ultrasonic Testing

The impact specimens were also tested using ultrasonic (UT) scanning technique. UT scanning is based on the principle of exposing an object to a frequency range of greater than 20 kHz and looking at the deflected beam to determine the size, shape, and location of defects. This study looks at the use of the UT C-scan. The C-scan is a two-dimensional presentation of defect distribution, displaying the size and position of the flaws in an area parallel to the surface through the raster scan of two axes (Kim and Liaw, 1998). The C-scan operates using a through-transmission mode, given in Figures 3.18. A specimen is placed in an immersion tank and a transmitting and receiving transducer are aligned together and perpendicular to the specimen. Then these transducers scan over the specimen. The sound waves amplitude lowers when it encounters defects within the specimen. Note that when this measurement is coupled with a time of flight, the depth of a flaw is indicated as well. Furthermore, the damage area can be caculated by looking at the levels of attenuation.

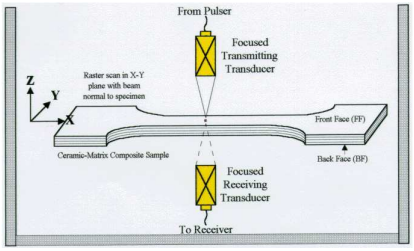

FIGURE 3.18: UT Scanning Through the Thickness Transmission Set-up

For this study, a C-scan was performed on each of the specimens by MSC. An example of the C-scan for specimen T17 is given in Figure 3.19.

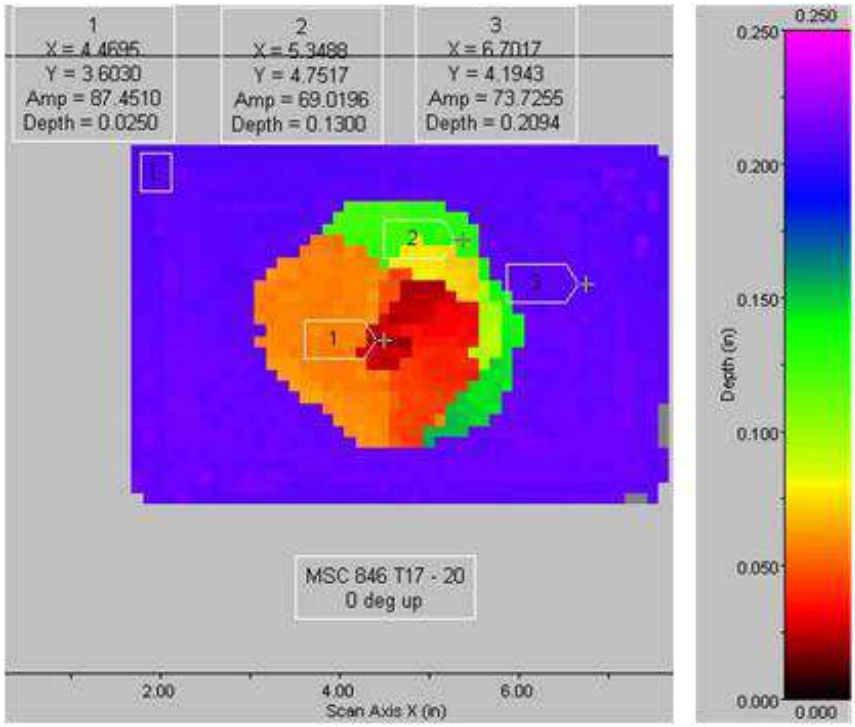

FIGURE 3.19: C-scan Image of Specimen T17

4

Numerical Validation

4.1 Finite Element Modeling

The impact specimens were modeled using a simplified version of the support base set-up given in Figure 4.1. In the model, the bottom of the specimen support plate is assumed rigid, therefore it is fixed in all six degrees of freedom. Furthermore, in order to model the clamping conditions, the tops of the clamps are fixed in all translational degrees of freedom. The contact between the clamps and the specimen, the support plate and the specimen, and the tup and the specimen is defined as surface to surface contact with the slave surface always specified as the specimen. The clamps and support plate were defined as having elastic deformable material properties of rubber and aluminum. In all cases, the tup is defined to be a rigid shell with an associated inertia to model the weight of the impact and an initial velocity. A representative mesh of the model is given in Figure 4.2.

For this study, three material models were analyzed for each impact energy level. These four models were: Chang-Chang model, Chang-Chang/Tsai-Wu model, and the Faceted Failure Surface Model. (It should be noted that initially this study set

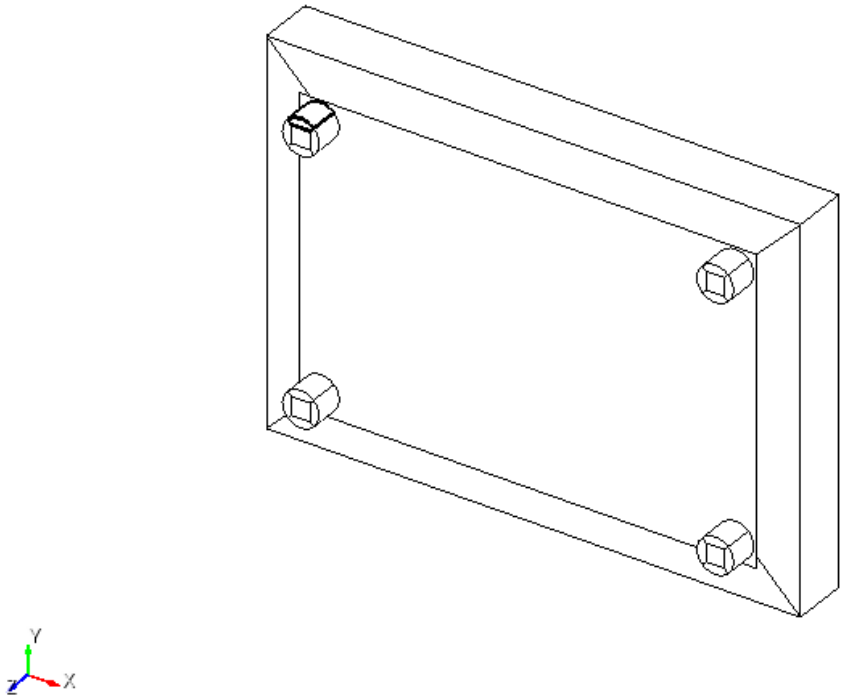

FIGURE 4.1: Finite Element Model of Support Base and Specimen

out to analyze the solid Hashin model, MAT_162, as well. However this model could not be used due to the formulation of the model. This model was not used because it is only available in an explicit formulation for solid brick elements, therefore under the dynamic loading with one element per ply the critical time step allowed by the program is exceeded.) The material input for the models is taken from Jumbo and are given in Table 4.1 (Jumbo et al., 2007). (Note the exact material card inputs are given in Appendix B.)

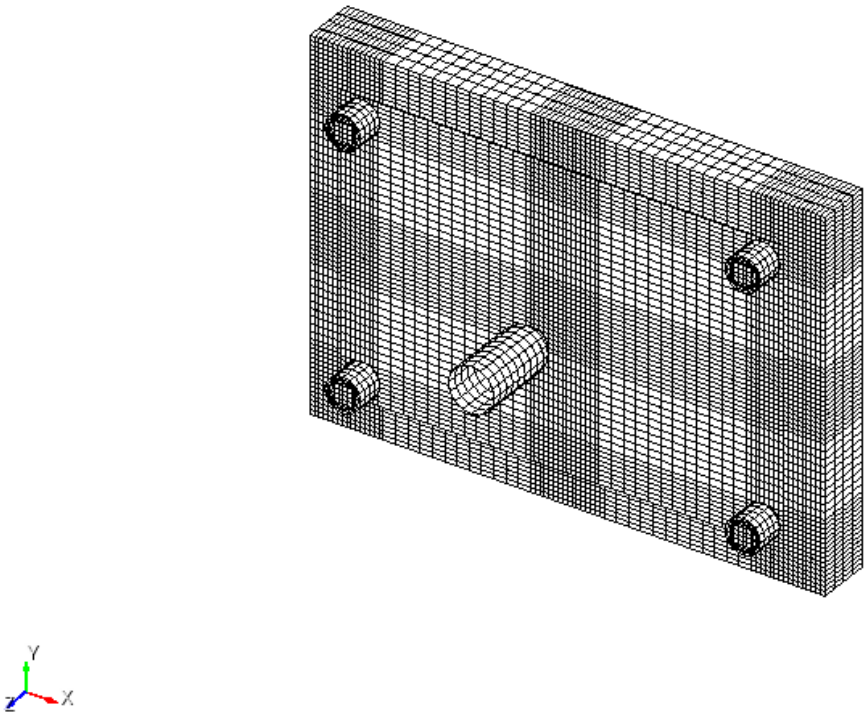

FIGURE 4.2: Finite Element Model Mesh

Table 4.1: Carbon Fiber Material Properties Used in Model Input

Material Property	**Value**
E_1	165 GPa
E_2	11.38 GPa
G_{12}	5.12 GPa
ν_{21}	0.021
S_c	90 MPa
X_c	1500 MPa
X_t	2600 MPa
Y_c	290 MPa
Y_t	60 MPa

Material model element deletion in both the case of the Chang-Chang model and Chang-Chang + Tsai-Wu model is based on setting the default values for softening factor equal to 1 and and the reduction factor for compressive fiber strength after matrix failure equal to 2. For the faceted failure surface, the progressive failure was based on the default strength reduction factor of 0.447. Therefore, the material yields at the corresponding failure strength value times the strength reduction factor. After yielding, the next yield point is based on the on the progressive failure descibes in Chapter 2 with a softening factor of 0.

4.2 Force, Displacement, and Energy Results

This section displays the results of the force and displacement curves for each of the impact specimens. Initially, all the displacement results are given, and these results are followed by all the force results. Note the displacement result for the FEA models is based on the nodal displacement of the bottom center node of the impactor. Also, the force result is based on the nodal force of the impactor. The impactor surface was chosen to correspond with the data acquired in the experimental results.

Note values are not given for the 12.5 ft-lb impact energy for the Chang-Chang failure model, because the model failed to converge due to reaching the critical time step set by the system. In looking at the plots and Table 4.2, the displacement results for the 16-ply specimens correspond well with those observed in the experimental data. For the 2.5 ft-lb specimens the distance from the average ranged from 0.02260 in to 0.2833. For the 5 ft-lb specimens the distance from the average ranged from 0.01673 to 0.02526. For the 7.5 ft-lb the distance from the average ranged from 0.01281 to 0.03504. For the 10 ft-lb the distance from the average ranged from 0.00336 to 0.02085. For the 12.5 ft-lb the distance from the average ranged from 0.05844 to 0.07564.

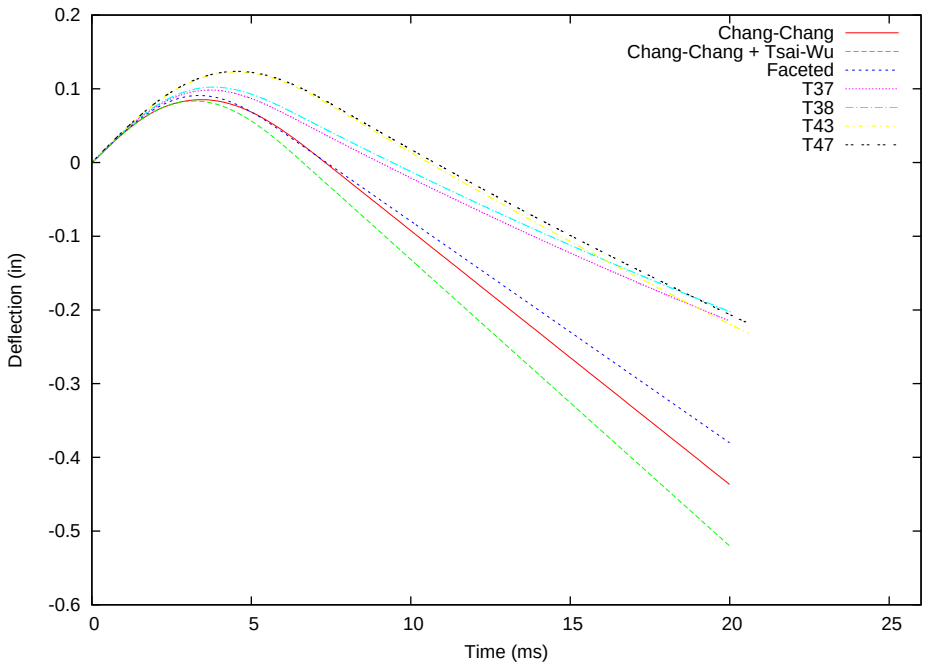

FIGURE 4.3: Deflection vs. Time for the 16-ply, 2.5 ft-lb Specimens (Note: As stated earlier, the displacement corresponds to the displacement of the bottom center node of the tup in the FEA model with the reference being the top of the specimen, which is positive downward. This value was chosen to best correspond with the position transducer in the experimental set-up which detects the position of the tup.)

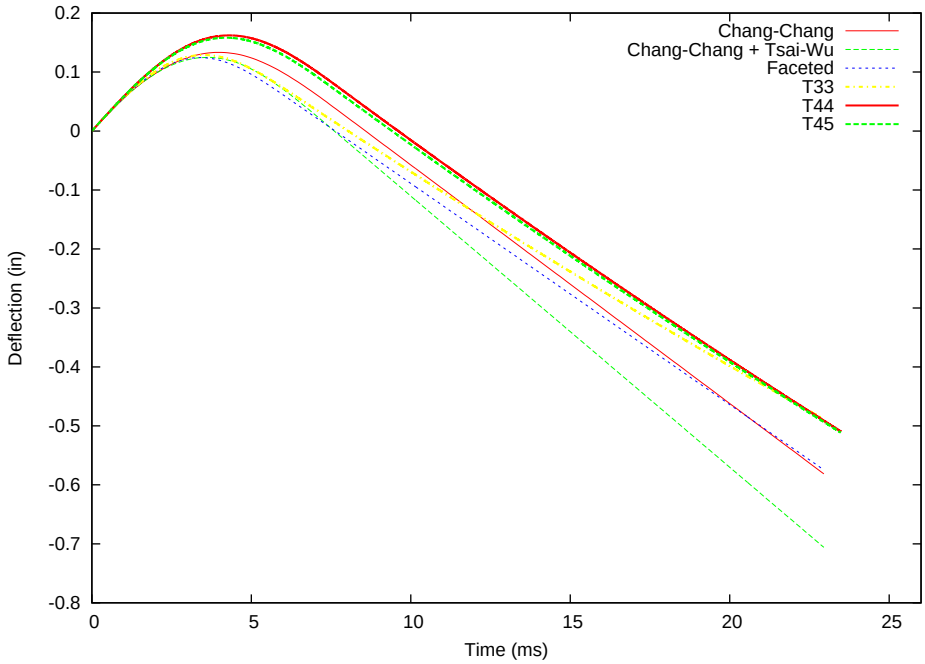

FIGURE 4.4: Deflection vs. Time for the 16-ply, 5 ft-lb Specimens

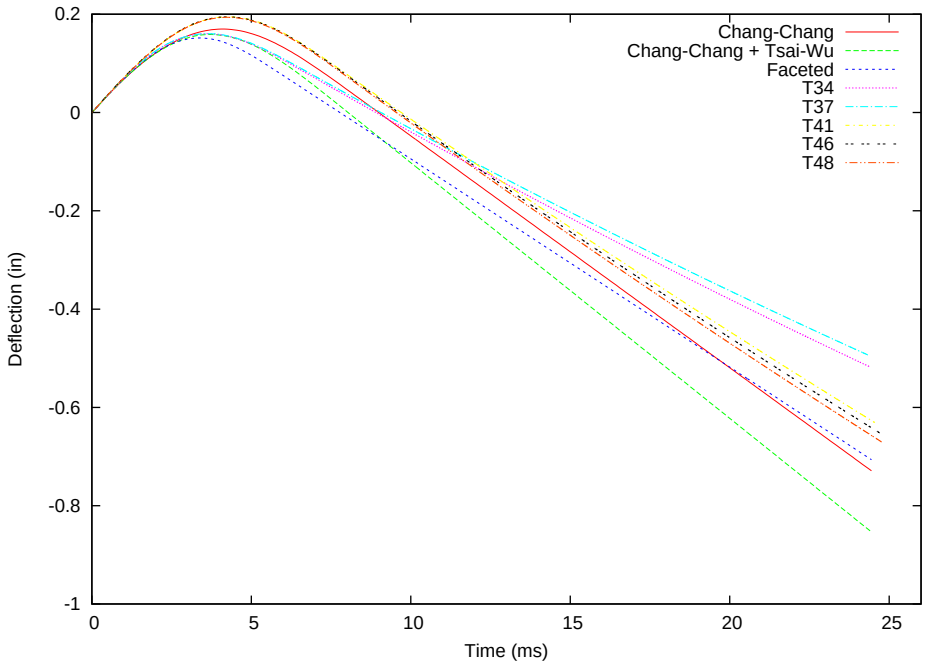

FIGURE 4.5: Deflection vs. Time for the 16-ply, 7.5 ft-lb Specimens

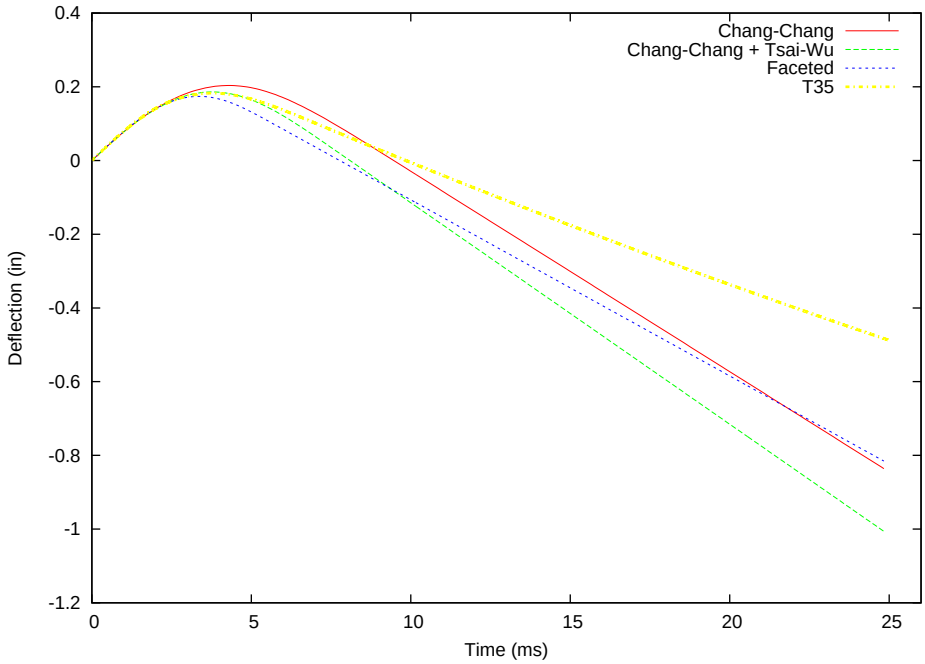

FIGURE 4.6: Deflection vs. Time for the 16-ply, 10 ft-lb Specimen

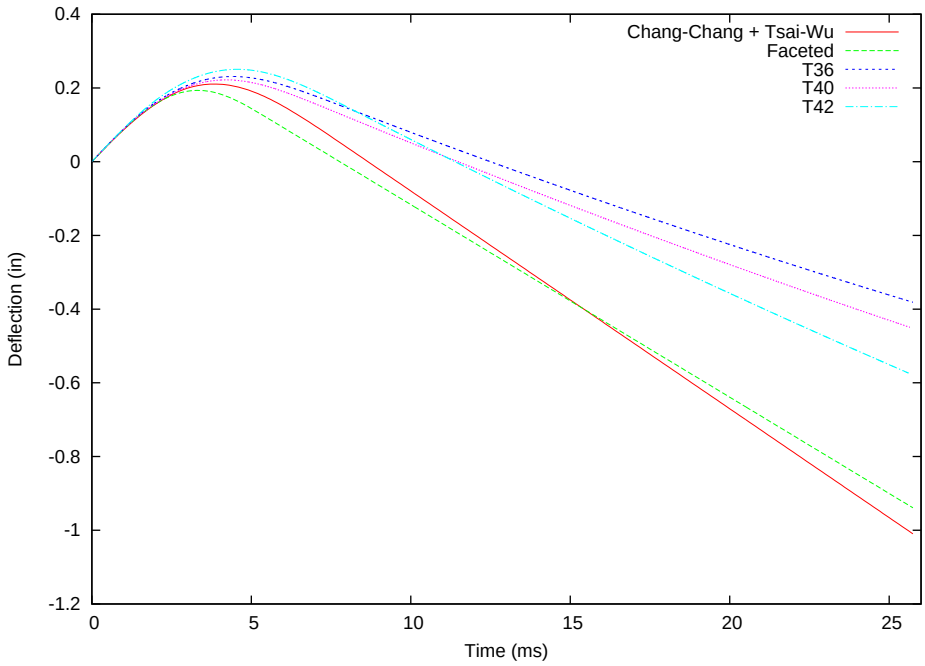

FIGURE 4.7: Deflection vs. Time for the 16-ply, 12.5 ft-lb Specimens

Table 4.2: Peak Displacement Results for 0.1025 in. Panels

Impact Energy (ft-lb)	**Test ID**	**Deflection (in)**	**Chang-Chang Result (in)**	**Chang-Chang + Tsai-Wu Result (in)**	**Faceted Result (in)**
2.5	T37	0.098267	0.08522	0.08335	0.09368
	T38	0.102242			
	T43	0.122561			
	T47	0.123657			
	Average	0.111628 ± 0.013302			
5	T33	0.128863	0.13336	0.12484	0.12447
	T44	0.16215			
	T45	0.158176			
	Average	0.14973 ± 0.01818			
7.5	T34	0.160303	0.16987	0.15867	0.15172
	T39	0.160506			
	T41	0.194727			
	T46	0.194656			
	T48	0.193714			
	Average	0.180981 ± 0.018797			
10	T35	0.182684	0.20353	0.18604	0.17405
12.5	T36	0.231016	na	0.158848	0.176043
	T40	0.221877			
	T42	0.250561			
	Average	0.234485 ± 0.014653			

This section depicts the 32-ply specimens displacement history.

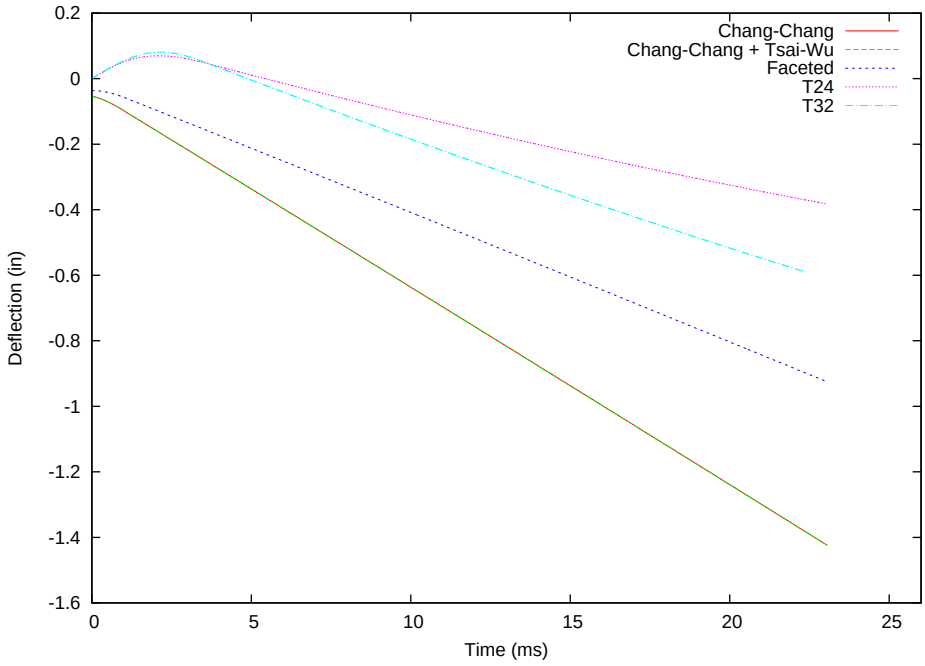

FIGURE 4.8: Deflection vs. Time for the 32-ply, 5 ft-lb Specimens

In Table 4.3, the reference point for the displacement is given as the top of the specimen in the initial configuration. Note that some of the values of the displacement are negative indicating they have never reached the zero value. These negative values are due to the contact algorithm with LS-DYNA. LS-DYNA implements a double pass penalty algorithm, meaning initially it calculates the spring force to push the slave surface to lie on the master surface. Then it reverses the definition of the slave and master surface and calculates a second spring force which is input into the global stiffness matrix. Due to this double pass penalty algorithm, the values of the displacement are far away from the experimental values expect for in the 40 ft-lb case.

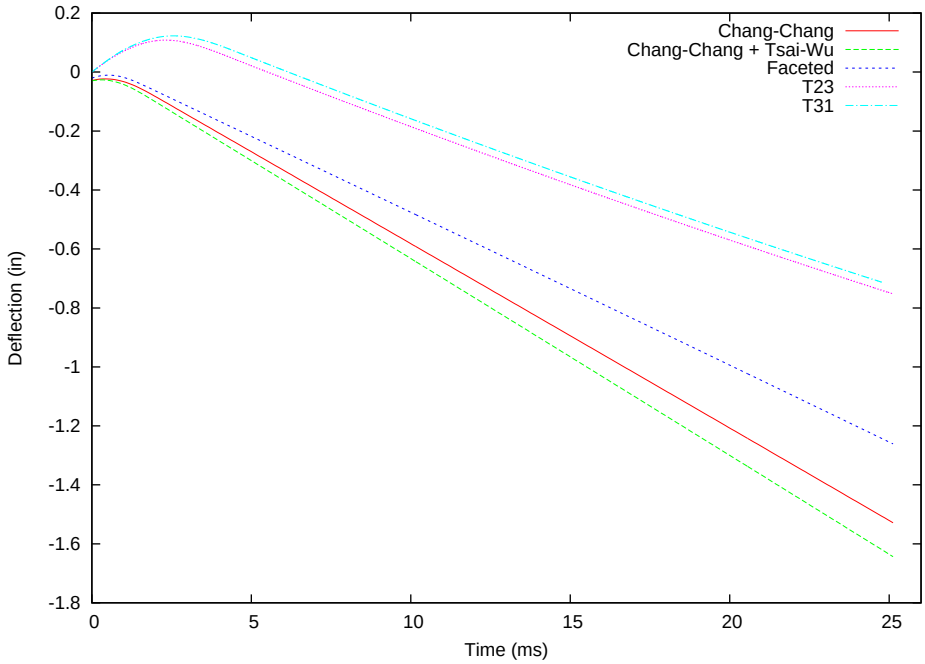

FIGURE 4.9: Deflection vs. Time for the 32-ply, 10 ft-lb Specimens

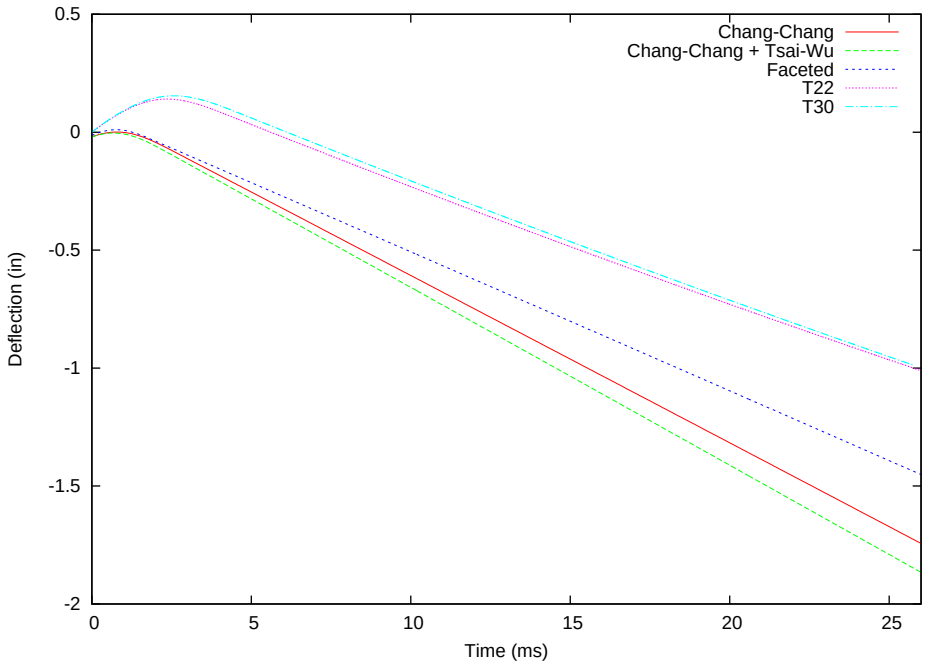

FIGURE 4.10: Deflection vs. Time for the 32-ply, 15 ft-lb Specimens

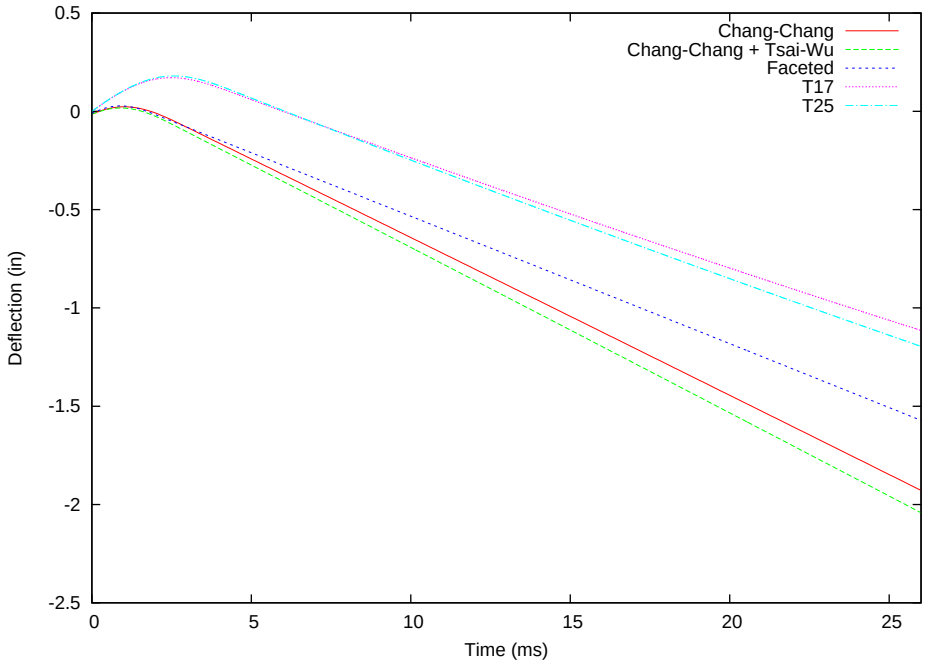

FIGURE 4.11: Deflection vs. Time for the 32-ply, 20 ft-lb Specimens

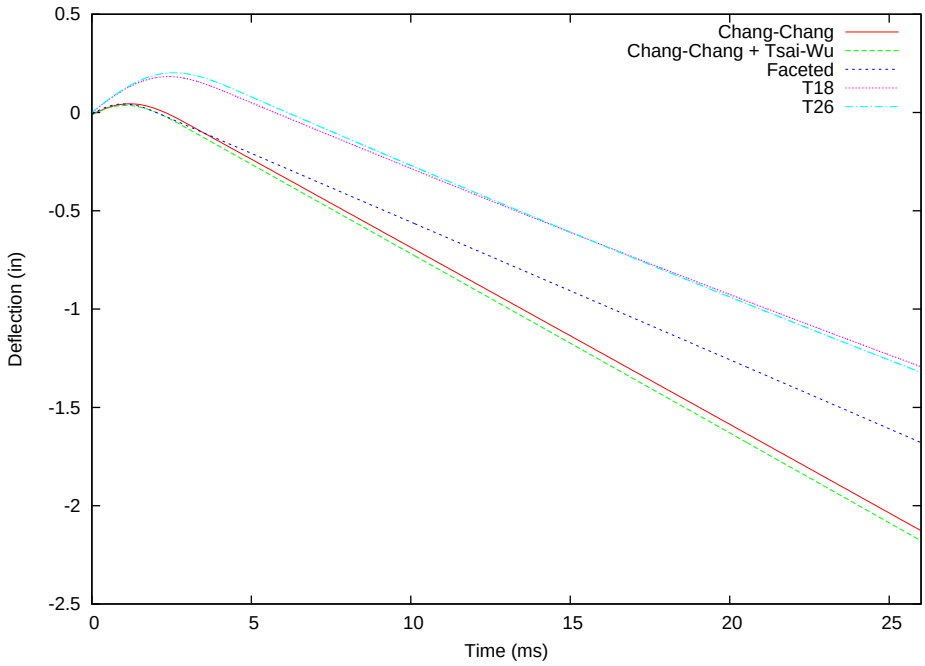

FIGURE 4.12: Deflection vs. Time for 32-ply, 25 ft-lb Specimens

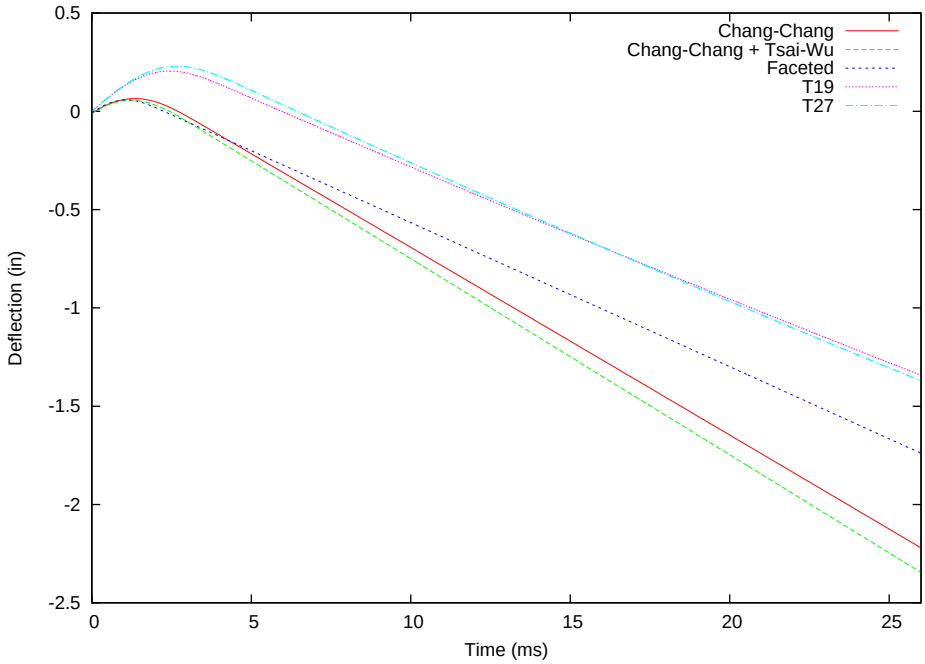

FIGURE 4.13: Deflection vs. Time for 32-ply, 30 ft-lb Specimens

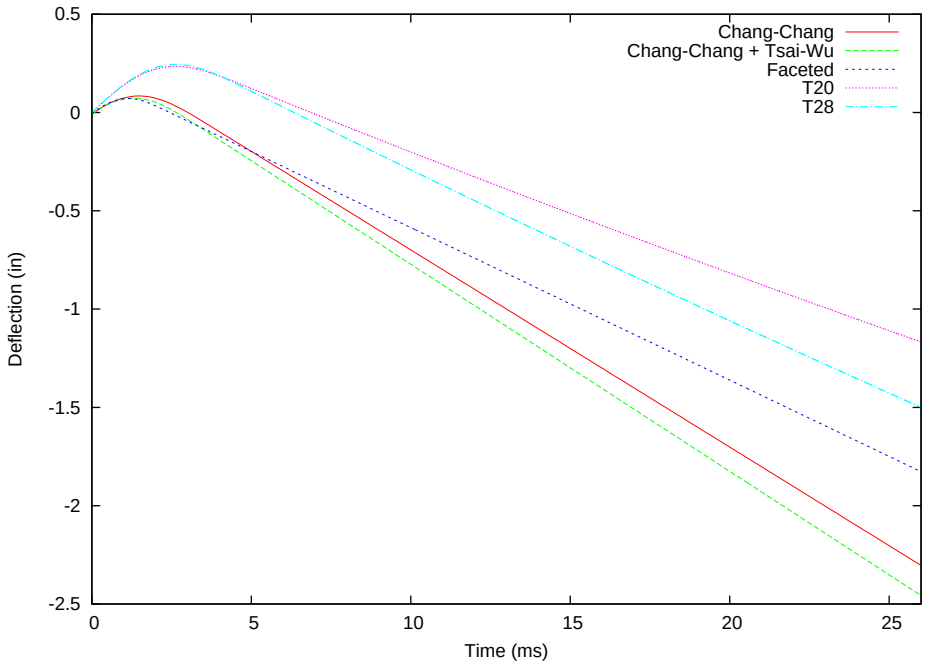

FIGURE 4.14: Deflection vs. Time for 32-ply, 35 ft-lb Specimens

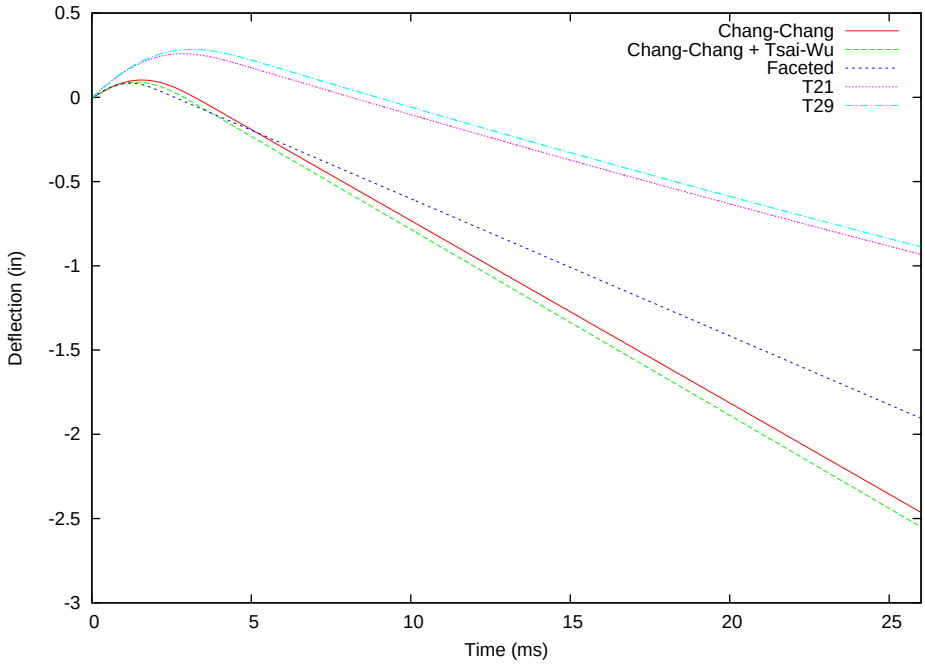

FIGURE 4.15: Deflection vs. Time for the 32-ply, 40 ft-lb Specimens

Table 4.3: Peak Displacement Results for 0.205 in. Panels

Impact Energy (ft-lb)	**Test ID**	**Deflection (in)**	**Chang-Chang Result (in)**	**Chang-Chang + Tsai-Wu Result (in)**	**Faceted Result (in)**
5	T24	0.069937	-0.05020	-0.05019	-0.03662
	T32	0.080816			
	Average	0.075377 ± 0.007693			
10	T23	0.108177	-0.02315	-0.02666	-0.01052
	T31	0.122684			
	Average	0.115431 ± 0.010258			
15	T22	0.140396	0.00054	-0.00360	0.01037
	T30	0.154238			
	Average	0.147317 ± 0.009788			
20	T17	0.171354	0.0231979	0.0170900	0.0277310
	T25	0.180132			
	Average	0.175743 ± 0.006207			
25	T18	0.182823	0.04424	0.03628	0.04363
	T26	0.20252			
	Average	0.192672 ± 0.013928			
30	T19	0.205099	0.06495	0.05646	0.05813
	T27	0.229579			
	Average	0.217339 ± 0.01731			
35	T20	0.234756	0.08402	0.07291	0.07154
	T28	0.244975			
	Average	0.239866 ± 0.007226			
40	T21	0.104396	0.10266	0.09155	0.08375
	T29	0.284188			
	Average	0.194292 ± 0.127132			

For this study, the displacements plot were used to gain insight in regards to energy, based on potential energy of the system. (This choice was made due to the fact that the experimental set-up caculates the energy through numerical integration. Hence, comparing a directly measured quantity was more desirable.) Therefore, in looking at the displacment plots, it should be noted that in general the numerical results do not deflect as far as the experimental results and the tup rebonds at a faster rate, meaning the numerical simulation is predicting a more elastic collision than the experimental results. The cause of the higher elasticity of the model can be attributed to one of two causes. The first being the material's behavior is predicted to be more elastic than reality. Since, the material models have an elastic-plastic nature, a greater elastic response indicates that the model predicts initial ply failure later than the experimental data. The second cause of a greater elastic response could be attributed to the double-pass penalty contact algorithm in LS-DYNA. As stated earlier, penalty contact implementation is like placing a spring in between the two contacting surfaces to enforce inpenetrability. Therefore, a spring force and corresponding spring energy are included in the calculation which is not included in the physical response of the system. This additional spring force will cause a more elastic rebound of the impactor and will add additional energy to the specimen, which can cause an overprediction of damage.

The next section depicts the results of the force for the 16-ply and 32-ply specimens. These results are given in Figures 4.16-4.28.

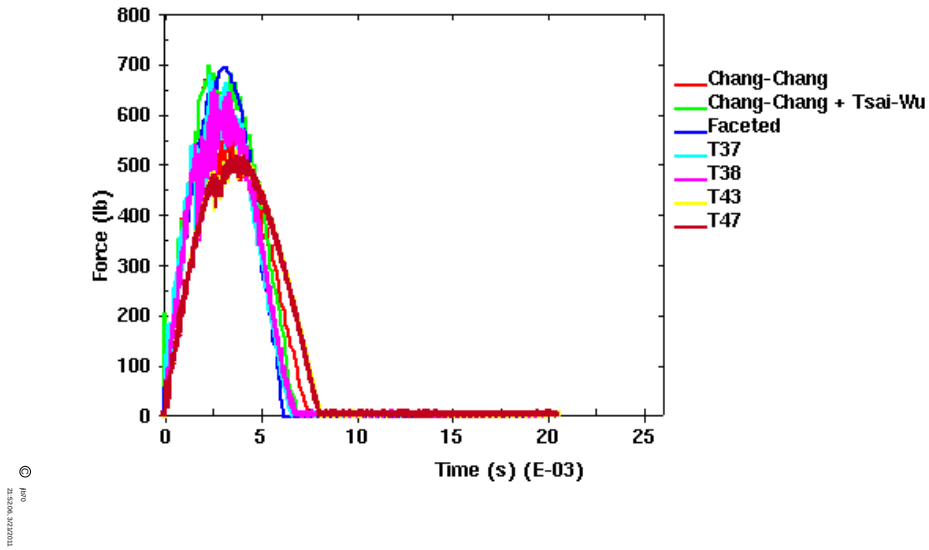

FIGURE 4.16: Force vs. Time for 16-ply, 2.5 ft-lb Specimens (Note: The force for the FEA results are the contact force of the tup, and the experimental results are based on a force transducer on the tup.)

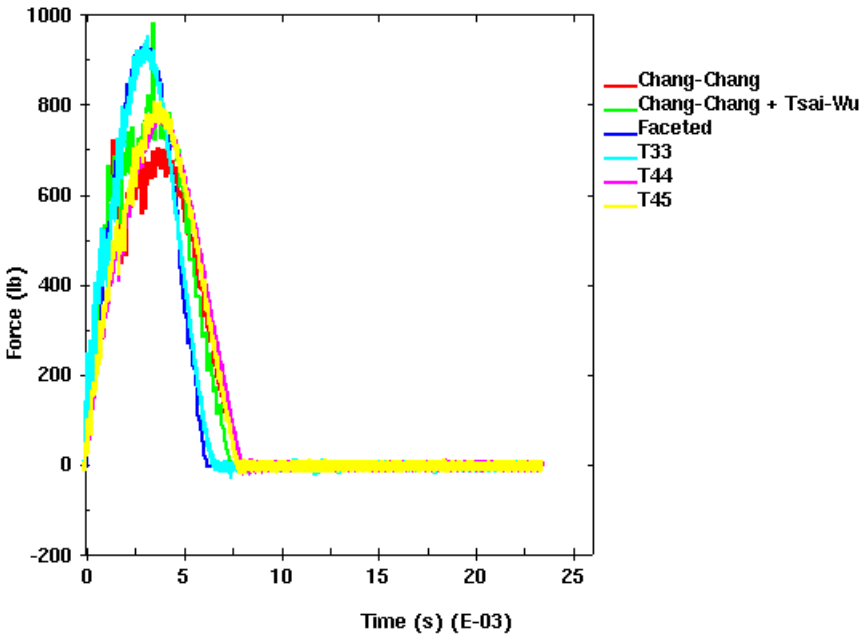

FIGURE 4.17: Force vs. Time for the 16-ply, 5 ft-lb Specimen

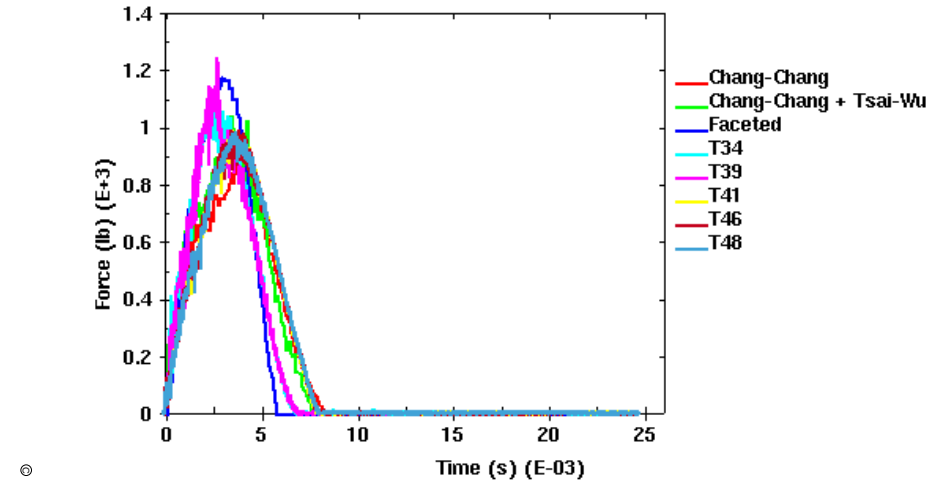

FIGURE 4.18: Force vs. Time for the 16-ply, 7.5 ft-lb Specimens

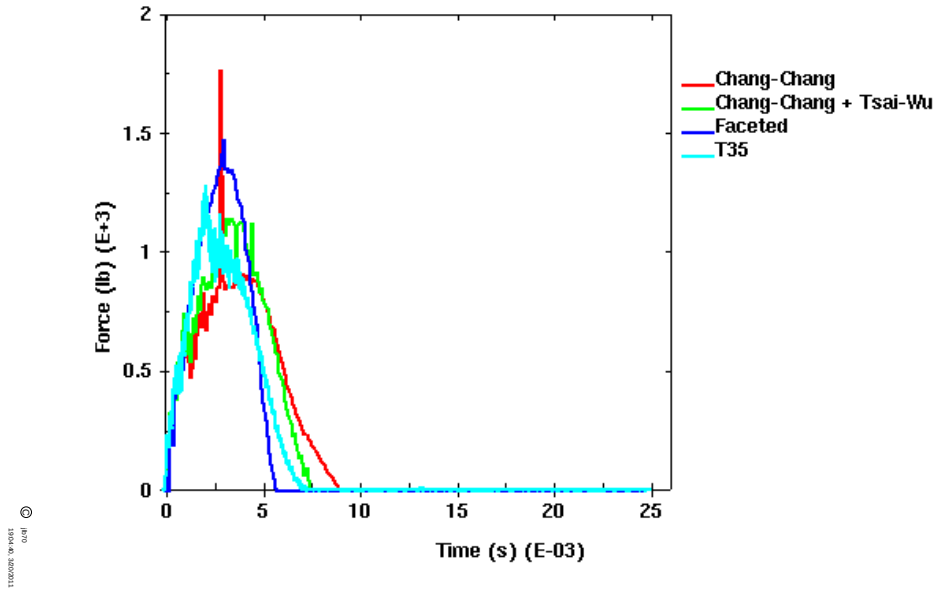

FIGURE 4.19: Force vs. Time for the 16-ply, 10 ft-lb Specimen

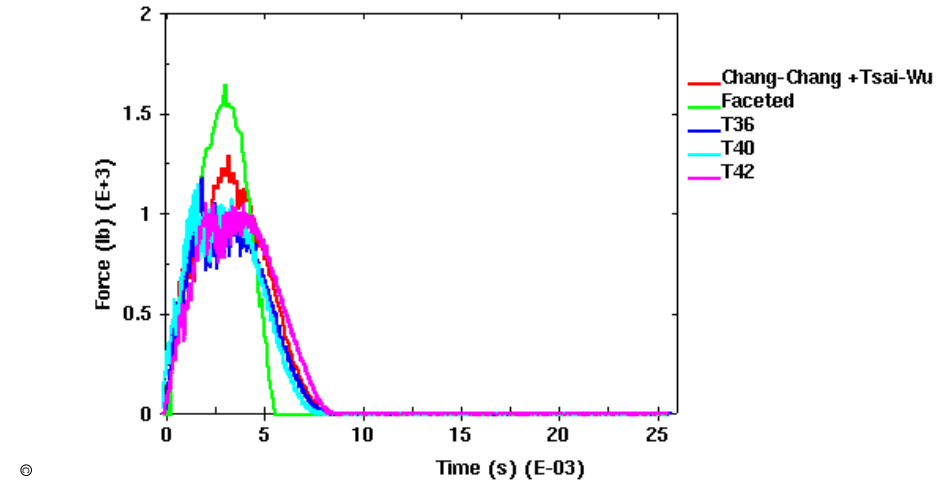

FIGURE 4.20: Force vs. Time for the 16-ply, 12.5 ft-lb Specimens

Table 4.4 summarizes the peak force results for the 16-ply specimens.

Table 4.4: Peak Force Results for 0.1025 in. Panels

Impact Energy (ft-lb)	**Test ID**	**Force (lb)**	**Chang-Chang Result (lb)**	**Chang-Chang + Tsai-Wu Result (lb)**	**Faceted Result (lb)**
2.5	T37	683.797	701.597	701.281	700.652
	T38	654.658			
	T43	532.067			
	T47	528.303			
	Average	599.7063 $\pm$ 81.1674			
5	T33	961.556	728.049	990.5	935.822
	T44	790.969			
	T45	812.774			
	Average	855.0997 $\pm$ 92.8363			
7.5	T34	1151.84	876.23	1045.49	1181.26
	T39	1249.48			
	T41	995.51			
	T46	996.432			
	T48	993.616			
	Average	1094.69 $\pm$ 113.5145			
10	T35	1285.87	1775.75	1151.17	1484.7
12.5	T36	1186.8	na	1300.92	1656.31
	T40	1157.77			
	T42	1060.83			
	Average	1135.133 $\pm$ 65.96533			

Table 4.4 depicts the force results for 16-ply specimens. These results in general are close to the average results for all the specimens. However, the faceted failure surface shows the highest result, except in the case the 10 ft-lb specimens.

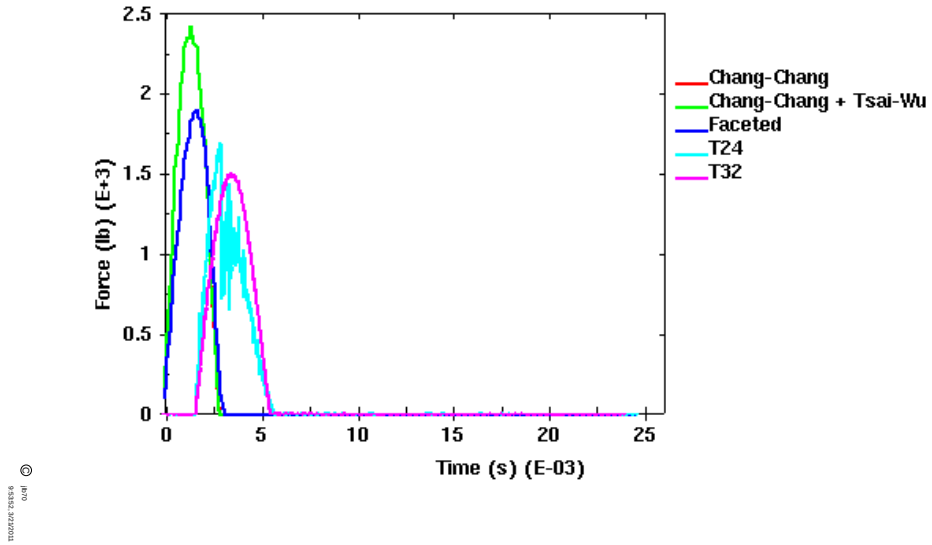

FIGURE 4.21: Force vs. Time for the 32-ply, 5 ft-lb Specimen

The next section show the force history plots of the 32-ply specimens.

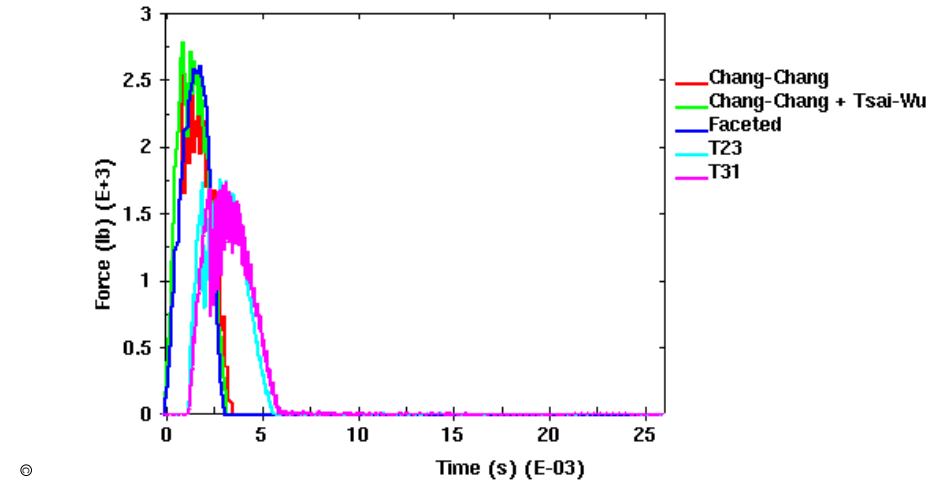

FIGURE 4.22: Force vs. Time for the 32-ply, 10 ft-lb Specimens

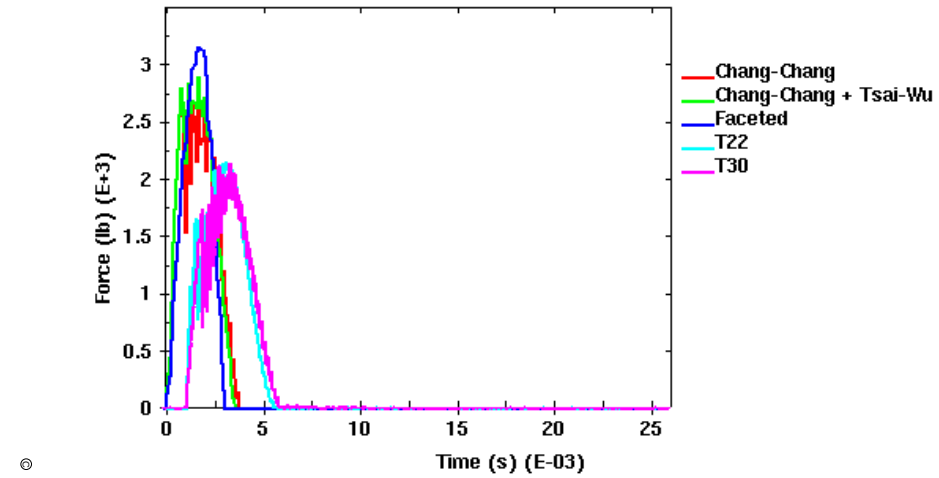

FIGURE 4.23: Force vs. Time for the 32-ply, 15 ft-lb Specimens

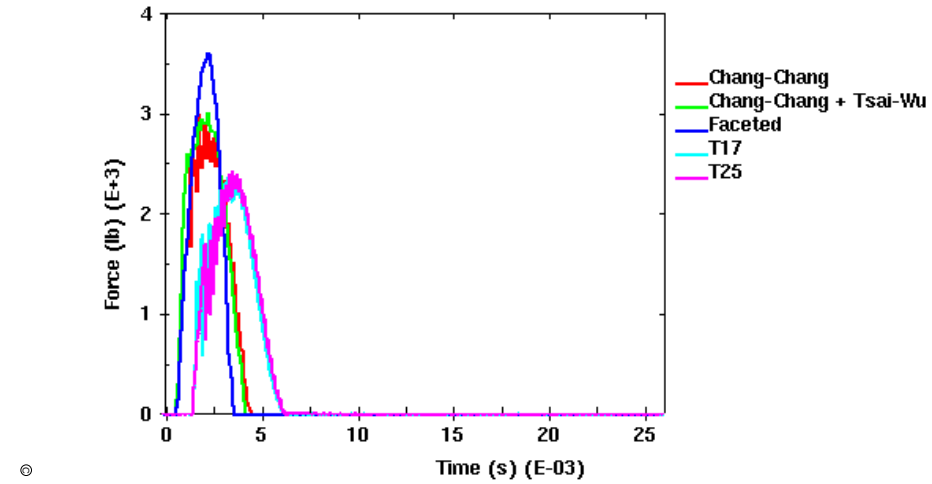

FIGURE 4.24: Force vs. Time for the 32-ply, 20 ft-lb Specimens

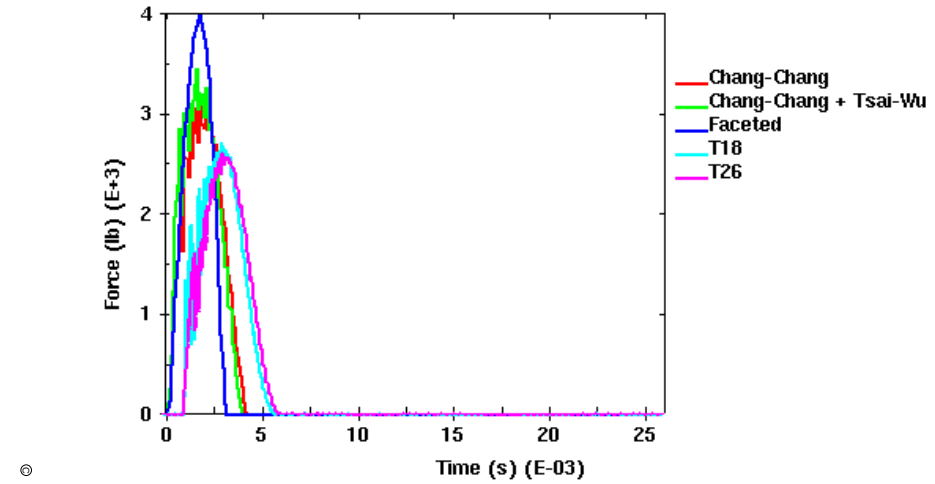

FIGURE 4.25: Force vs. Time for the 32-ply, 25 ft-lb Specimens

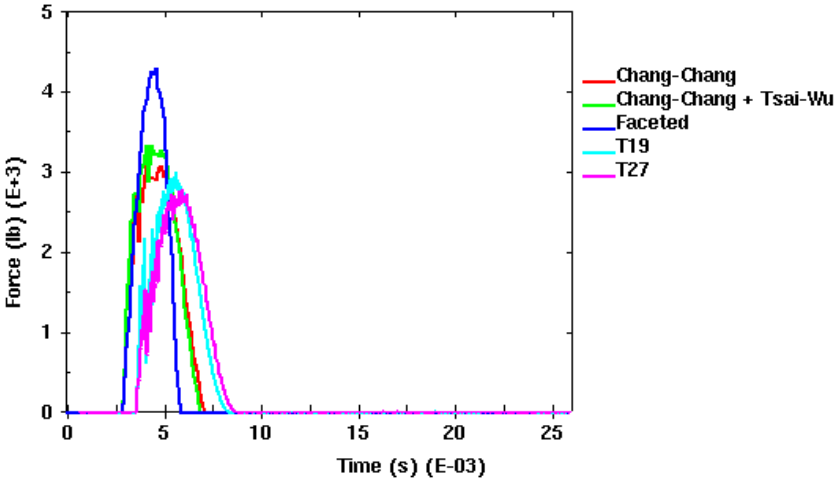

FIGURE 4.26: Force vs. Time for the 32-ply, 30 ft-lb Specimen

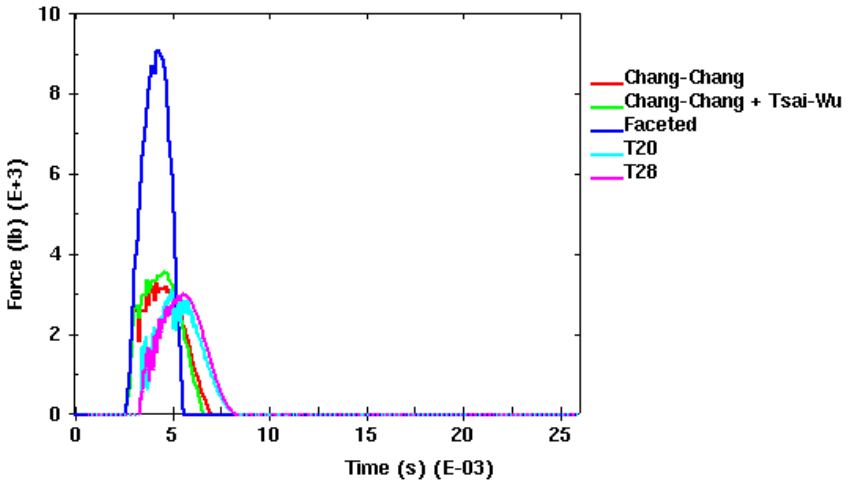

FIGURE 4.27: Force vs. Time for the 32-ply, 35 ft-lb Specimens

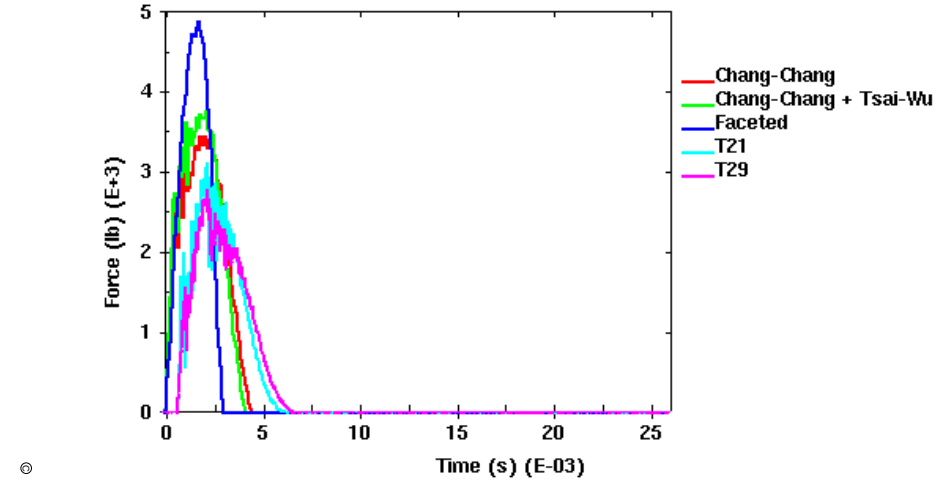

FIGURE 4.28: Force vs. Time for the 32-ply, 40 ft-lb Specimens

Table 4.5 summarizes the peak force results for the 32-ply specimens. From these results, the peak force of the models agrees well with the peak force of the experimental results.

Table 4.5: Peak Force Results for 0.205 in. Panels

Impact Energy (ft-lb)	**Test ID**	**Force (lb)**	**Chang-Chang Result (lb)**	**Chang-Chang + Tsai-Wu Result (lb)**	**Faceted Result (lb)**
5	T24	1699.38	2434.00	2434.11	1912.20
	T32	1518.51			
	Average	1625.445 ± 62.13347			
10	T23	1767.24	2682.35	2799.55	2624.57
	T31	1750.57			
	Average	1758.905 ± 11.78747			
15	T22	2158.613	2839.29	2909.05	3165.42
	T30	2149.21			
	Average	2153.912 ± 6.648925			
20	T17	2380.07	3014.06	3023.82	3617.75
	T25	2435.26			
	Average	2407.665 ± 39.02522			
25	T18	2722.07	3104.84	3469.70	3994.85
	T26	2614.59			
	Average	2668.33 ± 75.99984			
30	T19	3016.11	3147.35	3346.46	4317.90
	T27	2788.64			
	Average	2902.375 ± 160.8456			
35	T20	3153.91	3289.87	3579.92	9114.93
	T28	3018.98			
	Average	3086.445 ± 95.40992			
40	T21	2158.61	3464.17	3786.72	4895.62
	T29	2149.21			
	Average	2153.91 ± 6.64804			

This section shows looks at the energy results for the 16-ply and 32-ply specimens. In particular the section compares the net work in terms of the change in mechanical energy of the specimen.

$$W_d = \Delta KE + \Delta PE = 1/2mv_f^2 - 1/mv_{impact}^2 - (mgh_f - mgh_{impact}) \tag{4.1}$$

Note this work is defined in terms of the velocity of the tup and the displacement of the tup, therfore W_d is the net work done on the tup. If the work calculated by Equation (4.1) is negative then the tup has decreased in mechanical energy by adding work to the specimen. Therefore, the energy absorbed by the specimen, for this definition of work, is given by multiplying this W_d term by -1. A few representative plots are given to show the energy absorbed by the specimen in terms of the negative change in mechanical energy of the tup.

Therefore, from examining the plots of the difference in mechanical energy, experimental data shows that the specimen absorbs more energy than the numerical data. The cause of the material absorbing more energy in the experimental results than in the numerical results can be attributed to any of the following factors: the experimental results are capturing energy such as vibrational energy, frictional energy, ect. that is not captured by the model and cannot be considered negligible, or the experimental results are showing greater damage and the material model in the numerical results is underpredicting the damage.

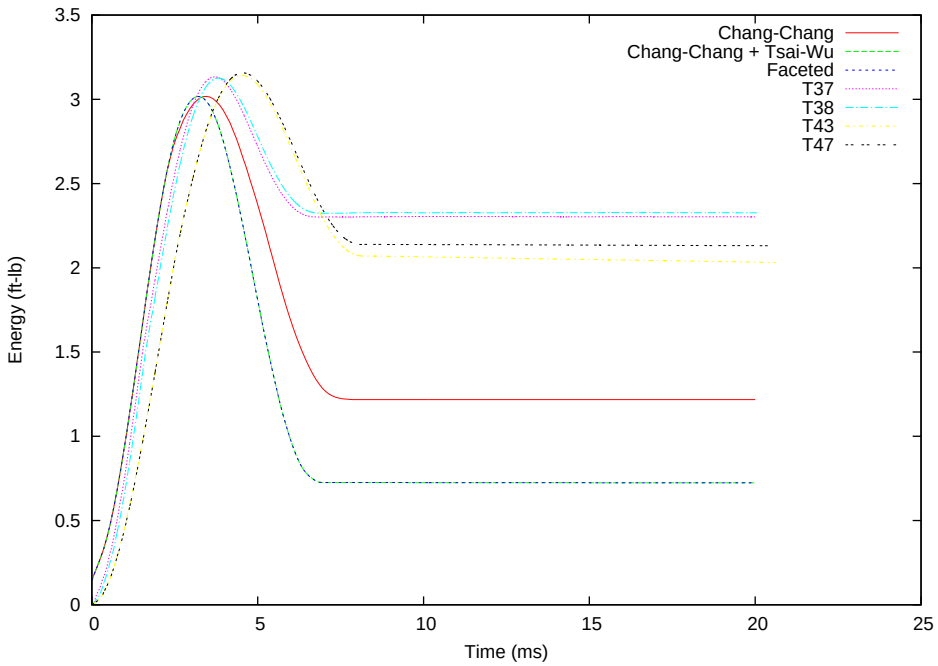

FIGURE 4.29: Mechanical Energy vs. Time for the 16-ply, 2.5 ft-lb Specimens (Note: The energy is calculated in the experimental results by calculating mechanical energy of the system based on the dropped mass and the velocity detector. For the FEA results, the energy is caculated in the same manner, with the dropped mass and the velocity of bottom center node of the tup.)

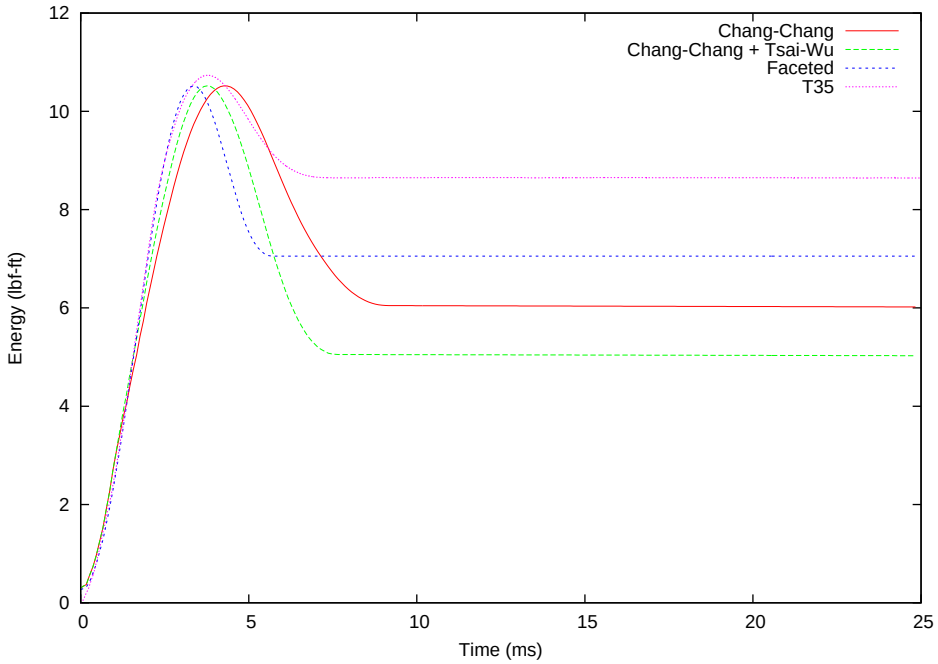

FIGURE 4.30: Energy vs. Time for the 16-ply, 10 ft-lb Specimens

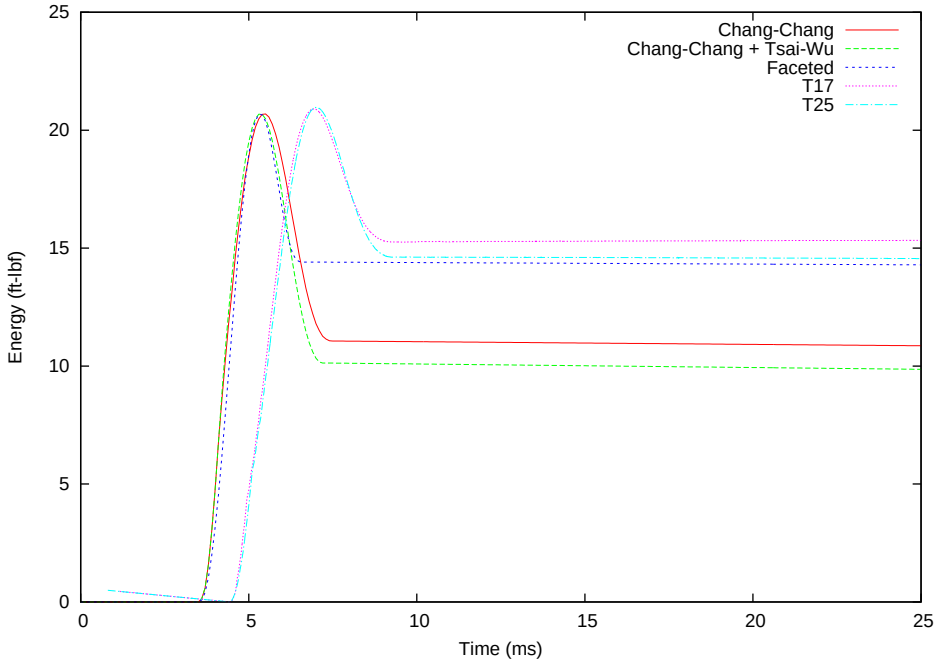

FIGURE 4.31: Energy vs. Time for the 32-ply, 20 ft-lb Specimens

4.3 Shearography, Thermography, and UT Results

In order to correlate with the shearography results, the measurement of the x-distance and y-distance related to the damage was taken from the shearography data, and the area was calculated based on the area of an ellispe. In the case of the thermography measure the area is based on the temperature distribution in the specimen with areas of defect having less thermal resistivity than areas without defects Chapter 3. In order to determine the damage area depicted in the model the von-Mises stress was contoured over the surface of the material. (Note: This choice was made based on the available choices of stress contours, as the value that would best represent a combined loading case.) The area for the numerical results was calculated within LS-DYNA using the function which measures the area. The results of the shearography, the thermography measurements, the UT measurements, and results for the model output are given in Table 4.6-4.7.

Table 4.6: Damage Area Results for 0.1025 in. Panels

Impact Energy (ft-lb)	**Test ID**	**SG Area** (in^2)	**UT Area** (in^2)	**Chang-Chang Area** (in^2)	**Chang-Chang + Tsai-Wu Area** (in^2)	**Faceted Area** (in^2)
2.5	T37	0.07	0.6013	0.9978	0.847081	5.16818
	T38	0.06	0.7854			
	T43	na	na			
	T47	0.05	0.4418			
5	T33	0.05	1.2272	1.72221	2.07642	11.1957
	T44	0.10	na			
	T45	0.16	0.7854			
7.5	T34	0.07	1.8005	6.13102	3.15345	14.5695
	T39	0.08	na			
	T41	0.08	1.2272			
	T46	0.07	0.9940			
	T48	0.08	1.2989			
10	T35	0.03	2.3224	3.19976	3.68486	16.718
12.5	T36	0.32	2.4557	na	4.30273	18.6532
	T40	0.19	2.3794			
	T42	0.23	1.9469			

Table 4.7: Damage Area Results for 0.205 in. Panels

Impact Energy (ft-lb)	**Test ID**	**SG Area** (in^2)	**TG Area** (in^2)	**UT Area** (in^2)	**Chang-Chang Area** (in^2)	**Chang-Chang + Tsai-Wu Area** (in^2)	**Faceted Area** (in^2)
5	T24	0.06	na	1.5469	7.9288	9.6669	3.8622
	T32	na	na	na			
10	T23	na	0.7019	3.0469	1.79379	1.28408	8.1913
	T31	0.04	0.5366	2.4053			
15	T22	0.68	1.3135	5.3438	3.0621	2.41694	11.4679
	T30	0.87	1.1170	3.1416			
20	T17	2.94	2.1190	7.9798	4.43899	3.234	17.4236
	T25	0.74	1.4330	5.0805			
25	T18	2.00	2.4511	7.669	4.67375	4.6369	20.5428
	T26	1.26	2.2007	7.0195			
30	T19	2.04	1.9782	8.2958	4.7019	4.80504	21.5623
	T27	1.09	2.2857	10.0625			
35	T20	1.57	2.1914	9.2806	6.51538	7.31329	23.1658
	T28	2.55	2.7173	9.6211			
40	T21	2.49	2.5221	8.2958	8.09728	11.5413	23.2448
	T29	0.87	3.1171	9.6211			

A representative case of the damage area from the FEA data and experiments are given in Figures 4.32.

In looking at Table 4.7, for higher impact energies, those above approximately 10 ft-lb, the shearography and thermography measurements provide similar results. However, the UT scan results are much higher in all cases due to the fact that the UT scan takes into account the depth of the damage. Therefore, the shearography and thermography scans are not adequate replacement for UT scans in regards the accurate measure of damage. Furthermore, the damage area related to the Faceted failure surface is significantly greater in all cases. This difference is due to the formulation of the failure criteria. The faceted failure surface is an example of an elastic-plastic model. The Chang-Chang and Chang-Chang + Tsai-Wu failure criterion both show results that are closer to the UT scan results.

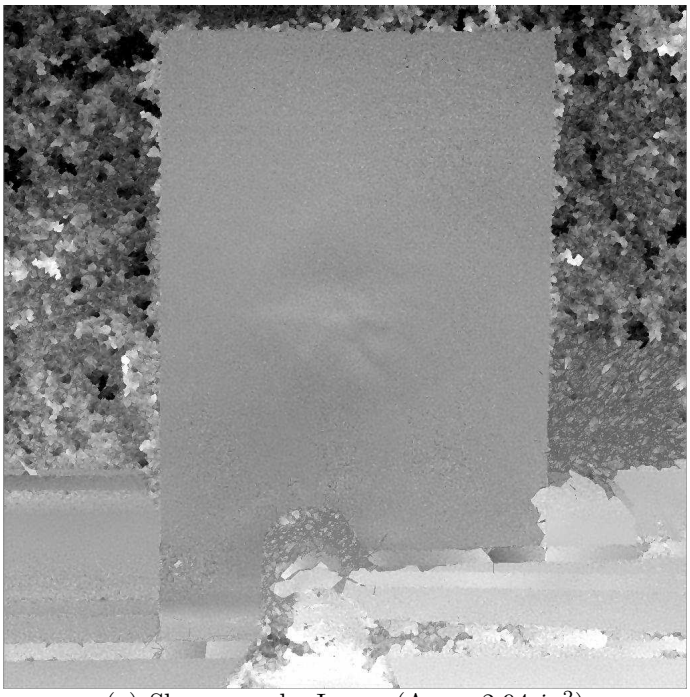

(a) Shearography Image (Area=2.94 in^2)

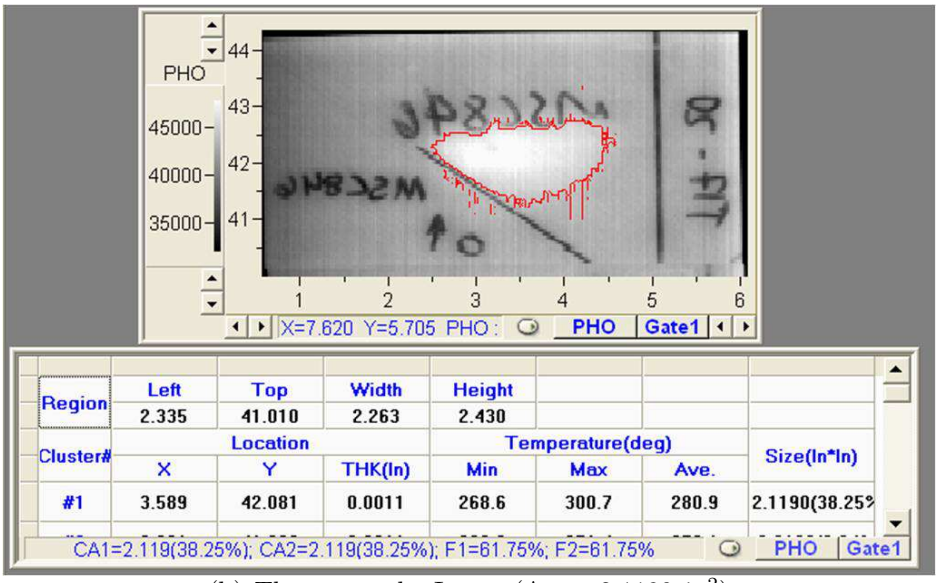

(b) Thermography Image (Area=2.1190 in^2)

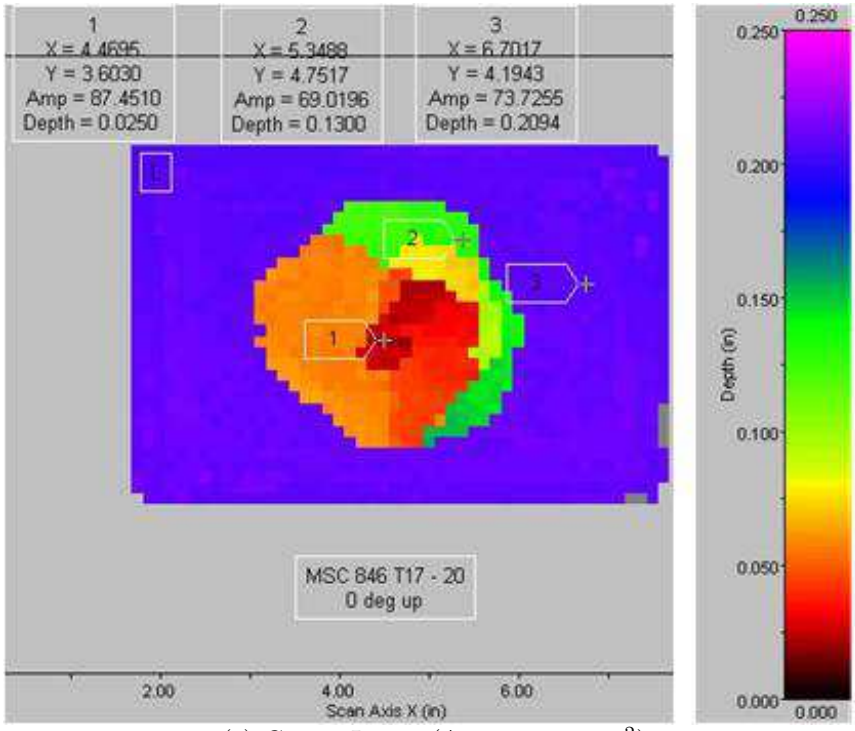

(c) C-scan Image (Area=7.9798 in^2)

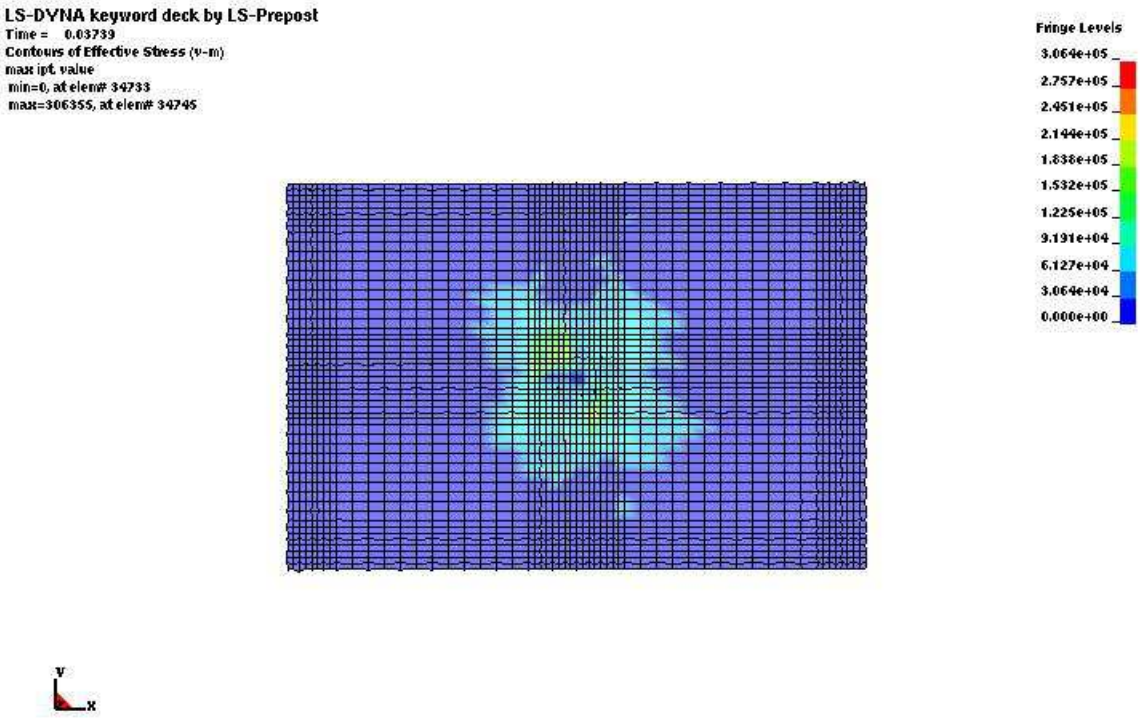

(d) Chang-Chang FEA Image (Area=4.43899 in^2)

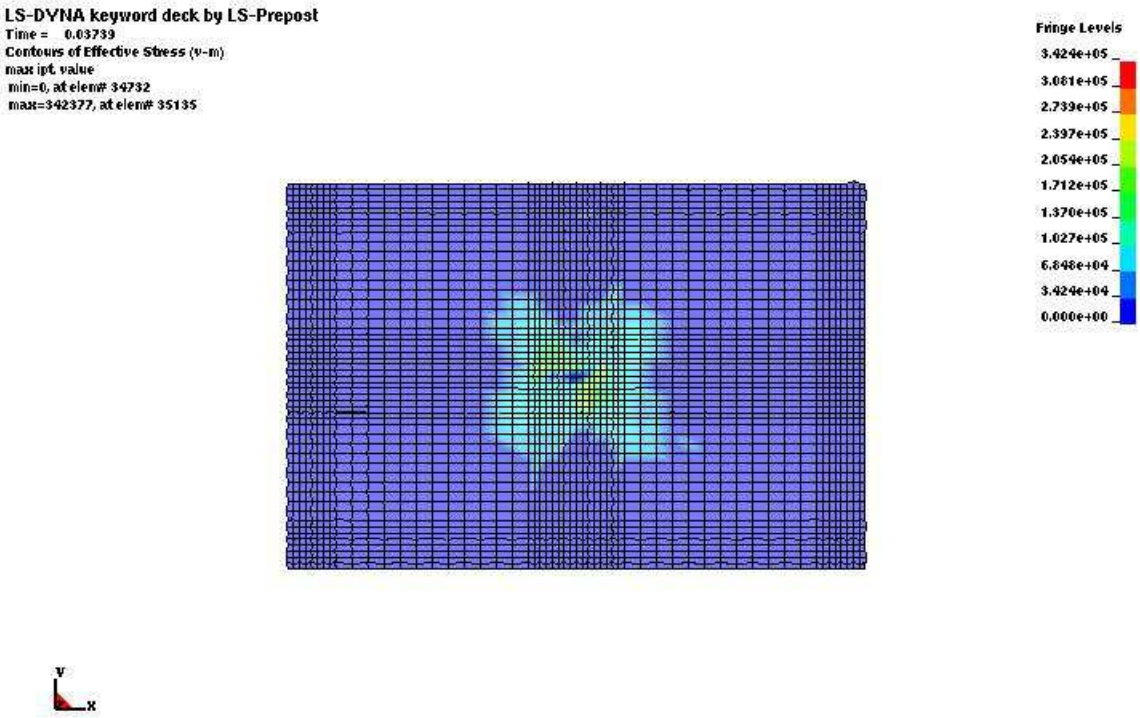

(e) Chang-Chang + Tsai-Wu FEA Image (Area=3.234 in^2)

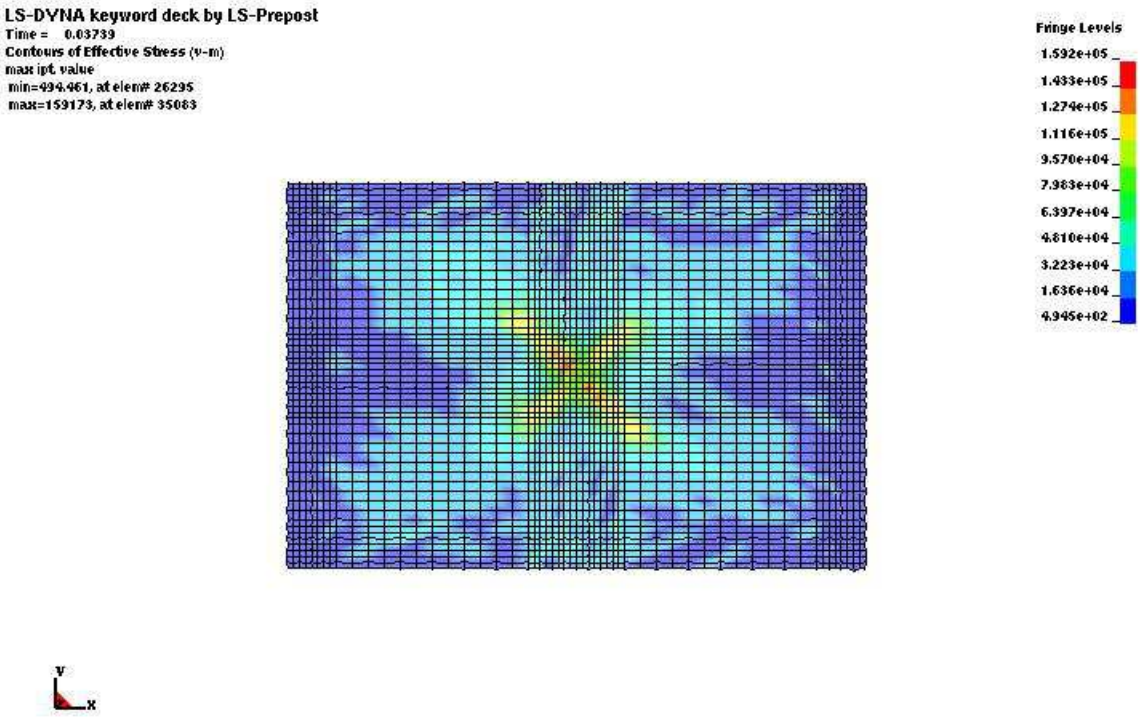

(f) Faceted Failure Surface FEA Image (Area=17.4236 in^2)

FIGURE 4.32: T17 Damage Area Comparisons

5

Conclusion

This study sought to determine whether current commercially available code was accurately able to predict impact damage of a carbon fiber composite material, and if this damage could be correlated with experimental results to develop a structural health monitoring system. The study showed that the three commercial models investigated gave an adequate correlation with the experimental force history. However the displacement history did not show adequate correlation for the 32-ply specimens due to the double-pass penalty method implementation. Overall the thermography and shearography do not provide as accurate of a measurement of damage area as the ultrasonic scans. In comparison to the NDE techniques, the faceted failure surface had the greatest damage area due to its elastic-plastic type formulation and its definition of initial ply failure. Furthermore, all models showed more elastic collision than the experimental results. This result can indicate that the models underpredict the damage in the material due to impact or that the contact implementation is adding energy to system to make the collision appear more elastic. Furthermore, the comparison of the mechanical energy results show that in the experiment specimen absorbs more energy than in the numerical results. Again, this result may have a

few causes: the model in underpredicting the damage, or model is not capturing every type of energy change associated with the experiment, like frictional loss or vibration energy. Therefore, the only conclusive statement is the FEA model is not accurately depicting what is happening in the experimental data. However, there is not a clear picture as to which part of the model is causing the inaccuracy, whether it is in the material formulation of damage or not. Therefore, the recommendations are for this specific material in development of a quality control system would be to do the following:

1. Investigate other commercially/non-commercially available progressive failure models to see if there is better correlation to the experimental results.

2. Investigate lower/higher impact energy levels, to define a threshold on each end where a progressive failure model prediction fails significantly.

The damage area is also still highly variable in relation to the finite element damage area, specifically for low impact energies. Therefore, the author suggests performing some destructive evaluation of the material, like hydrobrust testing in order to have a more quantitative evaluation of the predictive behavior of the material model itself in regards to energy.

In conclusion, these finite element models do not provide a suitable representation of impact damage. Ideally the study seeks to take data in the field, for example force data from an accelerometer, and use this data as inputs to a finite element simulation and predict where the localized stress would be. Also, the study seeks to look at the correlation between experiment and numerical results. This is done to seek out how well the numerical simulation models the type of damage. In theory, the experimental results for several load cases would be done, and correlated with many models. From this correlation, each model is evaluated on what which experimental data it models

the closet. Then each experiment is evaluated on what aspect of failure it predicts the best. From both of these evaluations, a judgement call can be made in regards to which structure would need to be decomissioned based on its intended use.

Appendix A

Appendix: Dynatup 9250HV Specifications

This section contains the specifications for some measured variables of the Dynatup 9250HV discussed in Chapter 3.

Dynatup 9250HV Specifications (Products, 2011):

- Force transducer type: strain gauge/piezo electric
- Measrurement of drop mass: electrical with strain gauge load cell
- Position rransducer: optical encoder
- Position accuracy: equal of less than +/−0.02mm(0.0008in) or +/−0.05% of displayed reading
- Position repeatability: +/−0.015 mm (0.0006 in)
- Speed accuracy: ±0.1% steady value
- Velocity detector display accuracy: ±0.25%
- Velocity accuracy: ±2% of set value

Appendix B

Appendix: Material Card Input

(Note the units here are the english units (in., lbf, ect.))

*MAT_ENHANCED_COMPOSITE_DAMAGE_TITLE

MAT_54

$# mid ro ea eb (ec) prba (prca) (prcb)

5 1.4260E-4 2.3900E+7 1.6500E+6 0.000 0.020000 0.000 0.000

$# gab gbc gca (kf) aopt

7.4000E+5 5.7000E+5 0.000 0.000 0.000

$# xp yp zp a1 a2 a3 mangle

0.000 0.000 0.000 0.000 0.000 0.000 0.000

$# v1 v2 v3 d1 d2 d3 dfailm dfails

0.000 0.000 0.000 0.000 0.000 0.000 0.000 0.000

$# tfail alph soft fbrt ycfac dfailt dfailc efs

0.000 0.000 1.000000 0.000 2.000000 0.000 0.000 0.000

$# xc xt yc yt sc crit beta

2.2000E+5 3.8000E+5 42000.000 8700.0000 13000.000 54.000000 1.000000

*MAT_ENHANCED_COMPOSITE_DAMAGE_TITLE

MAT_55

$# mid ro ea eb (ec) prba (prca) (prcb)

4 1.4260E-4 2.3900E+7 1.6500E+6 0.000 0.020000 0.000 0.000

$# gab gbc gca (kf) aopt

7.4000E+5 5.7000E+5 0.000 0.000 0.000

$# xp yp zp a1 a2 a3 mangle

0.000 0.000 0.000 0.000 0.000 0.000 0.000

$# v1 v2 v3 d1 d2 d3 dfailm dfails

0.000 0.000 0.000 0.000 0.000 0.000 0.000 0.000

$# tfail alph soft fbrt ycfac dfailt dfailc efs

0.000 0.000 1.000000 0.000 2.000000 0.000 0.000 0.000

$# xc xt yc yt sc crit beta

2.2000E+5 3.8000E+5 42000.000 8700.0000 13000.000 55.000000 1.000000

*MAT_COMPOSITE_FAILURE_SHELL_MODEL_TITLE

MAT_59

$# mid ro ea eb ec prba prca prcb

8 1.4260E-4 2.3900E+7 1.6500E+6 0.000 0.020000 0.000 0.000

$# gab gbc gca kf aopt maflag

7.4000E+5 5.7000E+5 0.000 0.000 0.000 1.000000

$# xp yp zp a1 a2 a3

0.000 0.000 0.000 0.000 0.000 0.000

$# v1 v2 v3 d1 d2 d3 beta

0.000 0.000 0.000 0.000 0.000 0.000 0.000

$# tsize alp soft fbrt sr sf

0.000 0.000 0.000 0.000 0.447000 0.000

$# xc xt yc yt sc

2.2000E+5 3.8000E+5 42000.000 8700.000 13000.000

Bibliography

Cawley, P. (1994), "The Rapid Non-Destructive Inspection of Large Composite Structures," *Composites*, 25, 351–357.

Center, L. R. (2011), "Scanning Thermography," `http://www.techbriefs.com/component/content/article/1036`.

Chang, F.-K. and Chang, K.-Y. (1987a), "Post-Failure Analysis of Bolted Composite Joints in Tension or Shear-Out Mode Failure," *Journal of Composite Materials*, 21, 809–833.

Chang, F.-K. and Chang, K.-Y. (1987b), "A Progressive Damage Model for Laminated Composites Containing Stress Concentrations," *Journal of Composite Materials*, 21, 834–855.

Hardy, G. and Bolen, J. (1989), "Thermal Inspection," *ASM Handbook: Nondestructive Evaluation and Quality Control*, 17, 396–404.

Hashin, Z. (1980), "Failure Criteria for Unidirectional Fiber Composites," *Journal of Applied Mechanics*, 47, 329–344.

Hashin, Z. and Rotem, A. (1973), "A Fatigue Failure Criterion for Fiber Reinforced Materials," *Journal of Composite Materials*, 7, 448–464.

Hinton, M., Kaddour, A., and Soden, P. (eds.) (2004), *Failure Criteria in Fibre Reinforced Polymer Composites: The World-Wide Failure Exercise*, Elsevier Science.

Incorporated, L. T. (2010), "Laser Shearography Technology," `http://www.laserndt.com/members/technology/shearography.htm`.

Jumbo, F., Ruiz, P. D., Yu, Y., Sawallowe, G. M., Ashcroft, I. A., and Huntley, J. M. (2007), "Experimental and numerical investigation of mechanical and thermal residual strain in adhesively bonded joints," *Strain*, 43.

Kim, J. and Liaw, P. K. (1998), "The Nondestructive Evaluation of Advanced Ceramics and Ceramic-Matrix Composites," *JOM-e*, 50.

Nguyen, M., Elder, D. J., Bayandor, J., Thomson, R. S., and Scott, M. L. (2005), "A Review of Explicit Finite Element Software for Composite Impact Analysis," *Journal of Composite Materials*, 39.

Okafor, A., Otieno, A., Dutta, A., and Rao, V. (2001), "Detection and Characterization of High-Velocity Impact Damage in Advanced Composite Plates Using Multi-Sensing Techniques," *Composite Structures*, 54.

Owens, A. and Jr., J. E. (2010), "Survivability of Composite Rocket Motorcases under Tactical Handling Condtions," in *AIAA Missile Sciences Conference*.

Products, I. I. (2011), "Dynatup 9200 Series Instrumented Impact Test Systems," `http://www.instron.com/wa/library/StreamFile.aspx?doc=99`.

Products, M. (2010), "Thermography Technology," `http://www.mistrasgroup.com/products/technologies/thermography.aspx`.

Růžek, R., Lohonka, R., and Jironč, J. (2006), "Ultrasonic C-Scan and Shearography NDI Techniques Evaluation of Impact and Defect Indentification," *NDT & E International*, 39.

Schweizerhof, K., Weimar, K., Münz, T., and Rottner, T. (1998), "Crashworthiness Analysis with Enhanced Composite Material Models in LS-DYNA - Merits and Limits," in *LS-DYNA World Conference*.

Steinchen, W. and Yang, L. (2003), *Digital Shearography Theory and Application of Digital Speckle Pattern Shearing Interferometry*, SPIE Press.

Tan, K., Watanabe, N., and Iwahori, Y. (2010), "Effect of Stitch Density and Stitch Thread Thickness on Low-Velocity Impact Damage of Stitched Composites," *Composites: Part A*, 41.

Thatte, B., Chandekar, G., Kelkar, A., and Chaphalkar, P. (2008), "Studies on Behavior of Carbon and Fiberglass Epoxy Composite Laminates under Low Velocity Impact Loading using LS-DYNA," in *10th International LS-DYNA User's Conference*.

Tsai, S. W. and Wu, E. M. (1971), "A General Theory of Strength for Anisotropic Materials," *Journal of Composite Materials*, 5, 58–80.

Yoder, N., Stites, N., Adams, D., Tripplett, M., and Esslinger, R. (2004), "Passive/Active Health Monitoring of Filament Wound Missiles," Tech. rep., Purdue University.